

Acoustofluidic bioassembly induced morphogenesis for therapeutic tissue fabrication

Received: 25 October 2023

Accepted: 7 April 2025

Published online: 05 May 2025



Byungjun Kang ^{1,14}, Eunseon Jeong ^{2,14}, Seung Yeop Han^{2,3},
Jeong Hyun Heo ⁴, Yunam Lee ¹, Suah Choi², Yunjung Choi¹,
Donyoung Kang ¹, Youn-Hoo Hwang¹, Jiin Lee², Jung Hwa Seo ⁵,
Jinyoung Kim^{5,6}, Inhea Jeong ⁷, Enji Kim ^{7,8}, Juyoung Lee¹, Dae-Eun Kim ¹,
Jang-Ung Park ^{7,8,9,10}, Sung-Rae Cho ^{5,6,11,12,13}, Yoonhee Jin⁴,
Seung-Woo Cho ^{2,8,10} ✉ & Hyungsuk Lee ¹ ✉

To build in vitro tissues for therapeutic applications, it is essential to replicate the spatial distribution of cells that occurs during morphogenesis in vivo. However, it remains technically challenging to simultaneously regulate the geometric alignment and aggregation of cells during tissue fabrication. Here, we introduce the acoustofluidic bioassembly induced morphogenesis, which is the combination of precise arrangement of cells by the mechanical forces produced by acoustofluidic cues, and the morphological and functional changes of cells in the following in vitro and in vivo cultures. The acoustofluidic bioassembly can be used to create tissues with regulated nano-, micro-, and macro-structures. We demonstrate that the neuromuscular tissue fabricated with the acoustofluidic bioassembly exhibits enhanced contraction dynamics, electrophysiology, and therapeutic efficacy. The potential of the acoustofluidic bioassembly as an in situ application is demonstrated by fabricating artificial tissues at the defect sites of living tissues. The acoustofluidic bioassembly induced morphogenesis can provide a pioneering platform to fabricate tissues for biomedical applications.

Fabrication of functional in vitro tissues is required for biomedical applications such as drug screening and regenerative medicine^{1–3}. Researchers have proposed that functional in vitro tissues can be constructed by mimicking the biological processes of morphogenesis that occur during embryonic development and tissue maturation^{4,5}. Two representative cellular processes are involved in morphogenesis: (1) arrangement of cells through cellular migration and (2) differentiation of cells with morphological changes⁶. For instance, morphogenesis induced by geometric and chemical cues in neuromuscular tissues dictates the unidirectional orientation of myogenic progenitor cells (MPCs) and the aggregation of cells through migration^{7–10} (Fig. 1a). Direct contact between aggregated

MPCs is required for the following processes, including the fusion and subsequent differentiation of multinucleated muscle cells^{8,11,12}. Axons of motor neurons (MNs) migrate to the membranes of muscle cells via chemical attractants^{13,14}, forming neuromuscular junctions (NMJs)^{15,16}. Tissues composed of co-aligned myofibers having NMJs play a critical role in directional voluntary contractions in response to electrical signals from the central nervous system. Therefore, to recapitulate the key functions of living tissues, it is necessary to replicate the high-resolution spatial arrangement and dense aggregation of cells^{17–20}.

Recently, diverse techniques have been developed for fabricating tissue constructs. Sphere-shaped cell aggregates called spheroids are

A full list of affiliations appears at the end of the paper. ✉ e-mail: seungwoocho@yonsei.ac.kr; hyungsuk@yonsei.ac.kr

effective in achieving the compactness of cells found inside *in vivo* tissues and organs^{21,22}. However, this approach has a limit mimicking the complex but ordered arrangement of cells specific to each organ. Extrusion methods using a nozzle can print cells into a designated position and construct 3-dimensional (3D) shapes^{23,24}. Volumetric optical printing can produce artificial tissues in which cells are arranged in a desired pattern by polymerizing a photosensitive hydrogel using light²⁵. These bioprinting fabrication techniques are advantageous for replicating complex patterns of cells. However, the application of bioinks containing high-density cells can negatively impact the printability, cell viability, and printing resolution of these methods^{26–28}, posing a challenge to increase the cell density and ensure

intercellular interactions that are crucial for the functional development of tissue.

In this study, we present the acoustofluidic bioassembly induced morphogenesis which consists of the replication of the cellular arrangement as occurred at the early phase of embryonic development using acoustofluidic bioassembly (AB) and the differentiation and morphogenesis of the arranged cells in the subsequent *in vitro* or *in vivo* culture (Fig. 1a). By utilizing acoustofluidic cues, such as acoustic pressure fields and fluidic fields²⁹, the acoustofluidic bioassembly method can effectively aggregate cells into the local minima of acoustic potential fields produced primarily by the scattering of pressure fields by cells³⁰. We developed an acoustofluidic device that is

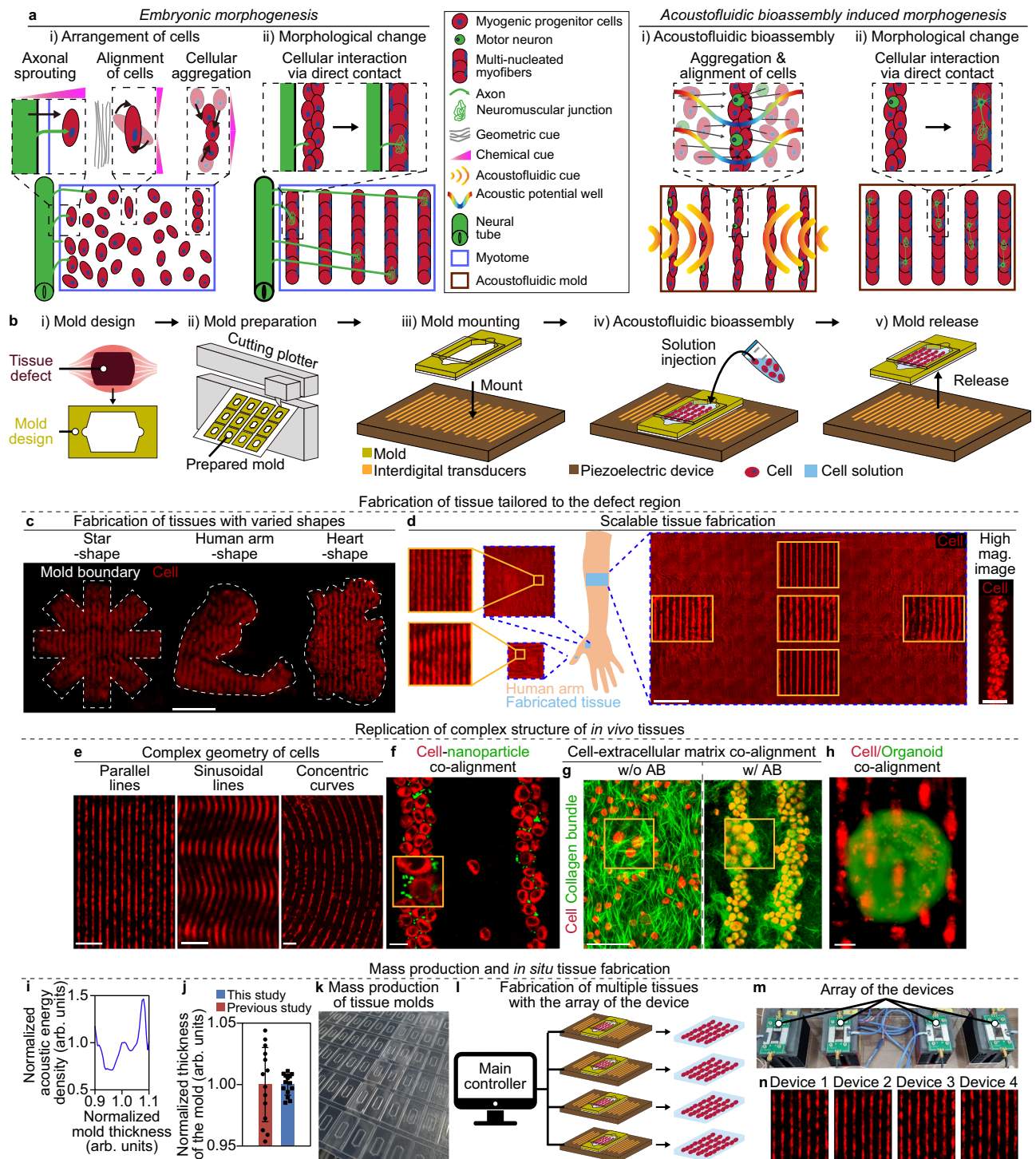


Fig. 1 | Fabrication of functional tissue constructs with the acoustofluidic bioassembly method. **a** Schematic of the cellular arrangement during embryonic (left) and acoustofluidic bioassembly (AB)-induced morphogenesis (right) in the neuromuscular tissues. Cellular morphogenesis followed by the acoustofluidic bioassembly can be conducted during *in vitro* or *in vivo* culture. **b** Schematic of the tissue fabrication using acoustofluidic bioassembly. **c** Fluorescent images of cells (red) arranged in a regular parallel line pattern in the tissue construct fabricated using the tissue molds having geometries including star, human arm, and heart. Scale bar represents 1 mm. White dotted lines represent the tissue mold boundary. **d** Schematic of fabricated tissue constructs in the mold placed on the human arm and a tile-scan fluorescent image of cells (red) of the entire tissue construct, and high-mag. image of cell aggregates at the center region. Scale bars in the tile scan and high-mag. images represent 5 mm and 50 μ m. **e** Fluorescent images of cells arranged into parallel and sinusoidal lines, and concentric curves. Scale bars

represent 0.5 mm. **f** Fluorescent image of cells (red) co-arranged with polystyrene polymer nanoparticles (green). Scale bars represent 20 μ m. **g** Fluorescent images of cells (red) and collagen bundles (green) in the tissues fabricated without (w/o) and with (w/) the AB. Scale bar represents 100 μ m. **h** Fluorescent image of cells (red) co-arranged with organoid (green). Scale bar represents 100 μ m. **i** Numerical analysis of the normalized acoustic energy density as the function of the normalized mold thickness. **j** Normalized thickness of the tissue molds in the previous³¹ and this study ($n = 14$ independent samples). Error bars represent a standard deviation. **k** Photograph of the mass production of the tissue molds. **l** Schematic of the fabrication of multiple tissues with the array of the tissue fabrication devices. **m** Photograph of the array of the devices. **n** Fluorescent images of cells (red) arranged at each device. Scale bars represent 100 μ m. Inset images within the solid orange rectangle in **(d)** and **(f)**, and **(g)** have been enlarged by 700%, 200%, and 200% in length, respectively. Source data are provided as a Source Data file.

able to construct tissues at varied dimensions and scales for therapeutic applications. We demonstrated that the macro-scale geometry of tissue, micro-scale pattern of cells, and interaction of nano-scale particles with cells could be regulated by the AB method. The aggregation of MPCs and MNs induced by acoustofluidic cues improved the fusion of muscle cells, differentiation of MPCs to contractile myofibers, and functional connections between muscle cells and neurons. *In vivo* tests of a mouse with volumetric muscle loss (VML) showed remarkable therapeutic efficacy of the neuromuscular tissue fabricated using the AB method, including structural and functional recovery of the mouse hindlimb. Finally, we demonstrate the potential use of the AB method for *in situ* applications by constructing muscle and neural tissues at damaged sites. The acoustofluidic bioassembly induced morphogenesis would be beneficial for biomedical applications such as drug screening and regenerative medicine.

Result

Acoustofluidic bioassembly method for tissue engineering

For ease of use, tissues were constructed inside a detachable mold designated to be fit to tissue defect (Fig. 1b). When a cell-laden hydrogel solution was injected into the mold mounted on the piezoelectric device, a surface acoustic wave was generated using interdigital transducers (IDTs) placed under the mold and transferred to the solution in the mold³¹ (Supplementary Fig. 1). Cells in the hydrogel solution were subjected to both acoustic radiation and drag forces and were located at the local minima of the acoustic potentials³⁰ (Fig. 1a). After the hydrogel was solidified, the mold containing the cell-laden gel was released from the device and transferred to a culture dish. Given that the acoustofluidic cellular arrangement occurred within tens of seconds³¹, the time required for tissue fabrication using the AB method would be determined by the gelation time of the hydrogel, which is independent of the size of the hydrogel.

Our AB method allowed 1) scalable fabrication of tissue tailored to the defect region, 2) replication of complex structure of *in vivo* tissues, and 3) mass production and *in situ* tissue fabrication which are essential for the clinical applications of fabricated tissues.

The scalable fabrication of tissues was facilitated by enabling the cellular arrangement in gel solution having geometries and size tailored to the defect site. By minimizing the acoustic interference using the solution-containing structure in the mold (Supplementary Note 1), our device could fabricate tissues with varied macro-structures, including stars, human arms, and hearts with cells exhibiting a regulated micro-pattern of parallel lines (Fig. 1c). Also, by placing IDTs in all areas that contact with the solution (Supplementary Note 2), we could fabricate the tissue construct in clinically-relevant sizes at the centimeter scale (Fig. 1d). A dense aggregation of cells into line patterns was exhibited in the entire region of the fabricated tissue (Supplementary Fig. 2).

Our technique can also help the replication of complex micro- and nano-structure of *in vivo* tissues. By combining complex shaped IDTs and modulation of frequency of electrical signals (Supplementary Fig. 3), we could arrange cells in simple parallel line patterns and other complex patterns, such as the sinusoidal patterns in the liver³² or the concentric curves in bone tissue³³ (Fig. 1e). The AB method could also regulate the nano-topography near cells through the label-free co-arrangement of cells with nanoparticles (NPs) of polymer (Fig. 1f). This approach could also be applied for various types of functional NPs such as gold and liposomes, which can help the upregulation of electrophysiological functions of cells³⁴ or the delivery of genetic materials to cells³⁵ (Supplementary Fig. 4). The bundles of collagen, a type of extracellular matrix (ECM) protein, could also be co-arranged with the cells (Fig. 1g and Supplementary Note 3), mimicking the structure of the perimysium of the skeletal muscle³⁶. The AB methods further enabled the patterning of single cells into specific geometric arrangements while positioning organoids between them (Fig. 1h and Supplementary Fig. 5). This would help simulate pancreatic or liver tissues where aggregation of islet cells or hepatocytes are placed between blood capillaries.

For mass production of tissues with high repeatability, it is desired to minimize the sample-to-sample variation in cellular arrangement. The acoustic properties, locations, and dimensions of device components such as the tissue mold, coupling material, and glass substrate are critical in determining the acoustofluidic fields^{37,38} (Fig. 1i). For this reason, we minimized a variation of rubber thickness that can be critical in determining acoustic field by using a rubber film of a constant thickness in creating the tissue mold³¹ (Fig. 1j). The mass production of the tissue molds was enabled by cutting the film with an automatic cutting machine (Fig. 1b and k). The array of the tissue fabrication device (Fig. 1l, m) combined with the tissue molds was used for the repeatable fabrication of the cell-arranged tissues (Fig. 1n and Supplementary Fig. 6).

Effects of direct cell-cell contact on tissue maturation

To evaluate the effects of the AB method on tissue maturation, neuromuscular tissues were fabricated using induced myogenic progenitor cells (iMPCs)^{39,40} prepared by direct cell reprogramming (Supplementary Note 4), primary motor neurons (pMNs), and Fibrin/Matrigel hydrogels^{41–43}. The number ratio of iMPC to MN was determined to be 200:1 based on the expression of myosin heavy chain (MHC), indicative of the degree of differentiation of iMPCs, in the co-culture experiment (Supplementary Note 5). The viability of cells in tissues fabricated with AB was comparable to those without AB (Supplementary Fig. 7). The tissues fabricated without AB and consequently containing randomly distributed cells were denoted as iMPC R (random) or iMPC+MN R, depending on whether the tissues consisted of solely iMPCs or a combination of iMPCs and pMNs. Tissues fabricated

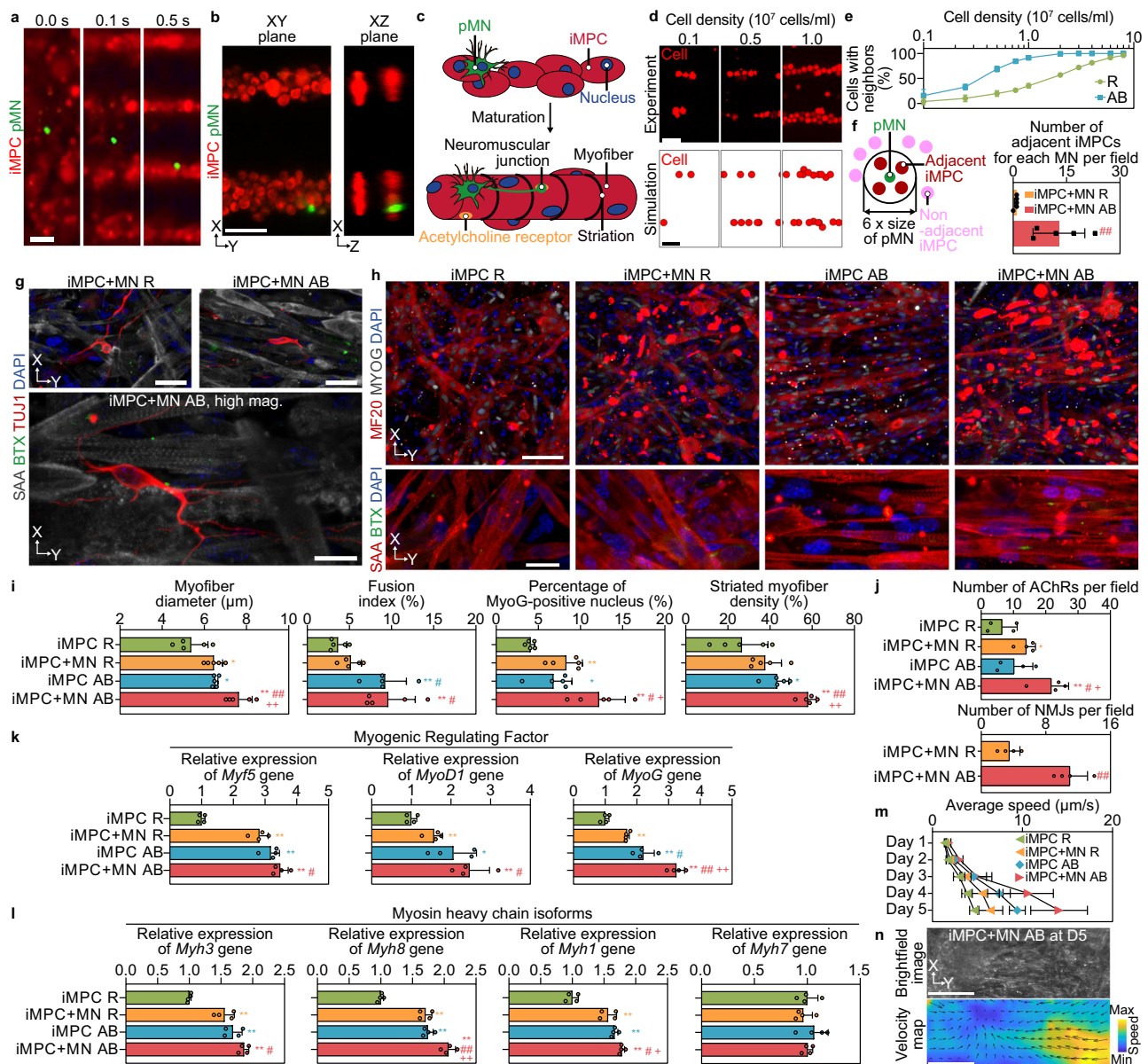


Fig. 2 | Effects of the acoustofluidic bioassembly on the maturation of neuromuscular tissue. **a, b** Time-lapse (**a**) and maximum intensity projection (**b**) fluorescent images of induced myogenic progenitor cells (iMPCs; red) and primary motor neurons (pMNs; green) under the acoustofluidic bioassembly (AB). Scale bar represents 50 μ m. **c** Schematic of the neuromuscular junction (NMJ) formation in the iMPCs and MNs after the AB. **d** Cellular distribution after the AB in the experiment and the simulation at various cell densities. Scale bars represent 50 μ m. **e** Numerical analysis of percentage of cells having neighbors in the tissue without (Random; R) and with the AB ($n=30$ independent trials). **f** Number of adjacent iMPCs per each pMN for iMPC+MN R and iMPC+MN AB groups ($n=5$). **g** Immunostaining images of SAA (gray)/BTX (green)/TUJ1 (red)/DAPI (blue) of iMPC+MN R and iMPC+MN AB groups. Scale bars in the upper and lower images represent 40 μ m and 20 μ m, respectively. **h** Immunostaining images for MF20 (red)/MyoG (gray)/DAPI (blue) (top) and SAA (red)/BTX (green)/DAPI (blue) (bottom) on day 5. Scale bars in the top and bottom row images represent 100 μ m and 20 μ m, respectively. **i** Average myofiber diameter, fusion index, percentage of MyoG-positive nucleus, and striated myofiber density ($n=5$ biologically independent samples). **j** Number of AChRs and NMJs ($n=4$ biologically independent samples). **k, l** qRT-PCR analysis of myogenic regulatory factors (**k**) and myosin heavy chain isoforms (**l**) on day 5 of iMPC R, iMPC+MN R, iMPC AB, and iMPC+MN AB groups ($n=4$ biologically independent samples). **m** Average cellular speed during spontaneous contraction on days 1, 2, 3, 4, and 5 ($n=4$ biologically independent samples). **n** Representative phase-contrast image (top) and velocity map (bottom) in iMPC+MN AB on day 5. Scale bars represent 100 μ m. All data are presented as mean \pm S.D., and statistical differences were determined with an unpaired, two-sided t-test. * $P < 0.05$ and ** $P < 0.01$ versus iMPC R, # $P < 0.05$ and ## $P < 0.01$ versus iMPC+MN R, and + $P < 0.05$ and ++ $P < 0.01$ versus iMPC AB. Source data are provided as a Source Data file.

with AB were referred to as iMPC AB and iMPC+MN AB, depending on the type of cells present in the tissues.

When acoustofluidic cues were applied, pMNs migrated slower than iMPCs (Fig. 2a and Supplementary Movie 1) and were positioned on the outer surface of the iMPC aggregates (Fig. 2b and c), as axons are found on the surface of skeletal muscles. The smaller diameter of

pMNs (Supplementary Fig. 8) would have reduced the acoustic radiation force, which might have led to their slower migration. To assess the impact of AB on cell-cell distance, we numerically estimated the 3D cellular distribution in tissues (Supplementary Note 6). The cell distribution obtained by numerical simulation was comparable to that observed in the experiment (Fig. 2d). AB increases the percentage of

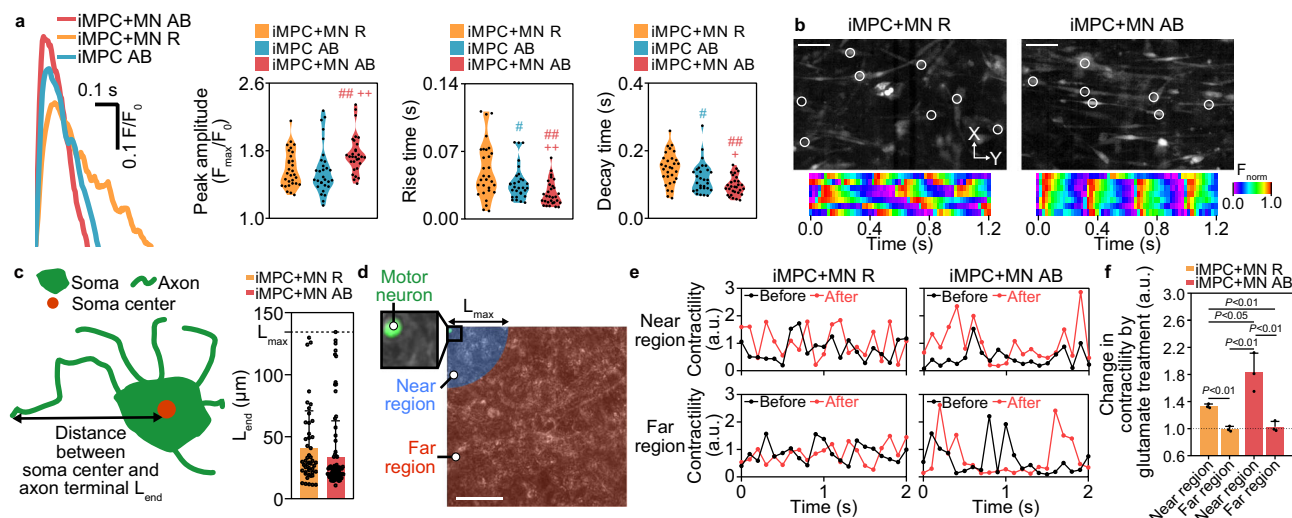


Fig. 3 | Electrophysiology characterization for neuromuscular tissue fabricated using acoustofluidic bioassembly technique. **a** Representative time-dependent calcium intensity of cells normalized by initial values (F/F_0), peak amplitude, and rise and decay time of the calcium signal in iMPC AB, iMPC+MN R, and iMPC+MN AB groups ($n = 30$). **b** Representative fluorescent images of Fluo-4 AM and normalized calcium intensity F_{norm} of cells in the regions delineated with white solid marks during the spontaneous contraction in iMPC+MN R and iMPC+MN AB groups. Scale bars represent 100 μm . **c** Schematic and the image-based analysis of the distance between soma center and axon terminal of motor neurons (L_{end}) in the iMPC+MN R and iMPC+MN AB group ($n = 47$ for iMPC+MN R and $n = 62$ for iMPC+MN AB). **d** Overlay of the brightfield image of the iMPC+MN R and the fluorescent image of a

membrane-stained motor neuron, with the definition of the near and far regions. Scale bar represents 50 μm . **e** Representative contractility of cells in near and far regions of iMPC+MN R and iMPC+MN AB group before and after the glutamate treatment. Contractility values were normalized to the average one before the glutamate treatment. **f** Change in contractility of cells in near and far regions of iMPC+MN R and iMPC+MN AB groups after glutamate treatment ($n = 3$ biologically independent samples). a.u., arbitrary units. All data are presented as mean \pm S.D., and statistical differences were determined with an unpaired, two-sided t-test. * $P < 0.05$ and ** $P < 0.01$ versus iMPC R, # $P < 0.05$ and ## $P < 0.01$ versus iMPC+MN R, and + $P < 0.05$ and ++ $P < 0.01$ versus iMPC AB. Source data are provided as a Source Data file.

the cells with neighbors within a distance of 1.5 folds of average diameter of cells due to its aggregation effect (Fig. 2e). AB also led to a significant increase in the number of iMPCs adjacent to pMNs, indicating that AB might enhance the direct physical interaction between iMPCs and pMNs (Fig. 2f).

We investigated the effects of AB on the morphology and genetic expression of cells in the fabricated tissues. Immunofluorescence images on day 5 showed that the neurites of pMNs, indicated by TUJ1 (neuron-specific class III beta-tubulin), in iMPC+MN AB sprouted along the surface of sarcomeric alpha-actinin (SAA)-positive iMPCs (Fig. 2g). We also observed that the pre-synaptic component axon was in contact with the post-synaptic component alpha-bungarotoxin (BTX)-positive acetylcholine receptors (AChRs) in skeletal muscle cells (Supplementary Fig. 9). In contrast, the pMNs randomly sprouted within the 3D hydrogel in iMPC+MN R. This suggests that cellular aggregation by acoustofluidic cues may be beneficial for the interactions between iMPCs and pMNs. Immunofluorescence images of iMPCs on day 5, revealed a greater number of Myogenin (MyoG)-positive cells and myofibers with sarcomeres, indicated by the periodic pattern of SAA, in iMPC AB and iMPC+MN AB groups than in iMPC R and iMPC+MN R groups (Fig. 2h). The image-based analysis showed that the diameter of myofibers, percentage of MyoG-positive nuclei, fusion index, and spatial density of striated myofibers were increased by the co-culture of iMPCs with pMNs and cellular arrangement by acoustofluidic cues (Fig. 2i). Compared to iMPC+MN R group, the number of BTX-positive AChRs and NMJs was significantly higher in iMPC+MN AB group (Fig. 2j). We further analyzed the expression of genes related to the differentiation and maturation of skeletal muscle cells using quantitative reverse transcription polymerase chain reaction (qRT-PCR). The expression of myogenic regulatory genes, such as *Myf5* (myogenic factor 5), *MyoD1* (myogenic differentiation 1), and *MyoG*, and MHC isoform genes, including *Myh3* (embryonic MHC), *Myh8* (neonatal MHC), and *Myh1* (fast adult MHC), were all

synergistically increased by the AB method and co-culture with pMNs (Fig. 2k and l). The expression of *Myh7* (slow adult MHC) was similar in all groups. These results suggest that the direct contact between iMPC and pMN induced by AB could promote the formation of NMJs, fusion, and consequential maturation of iMPCs.

We investigated the effects of the cellular arrangement mediated by the AB method on the contractile and electrophysiological functions of tissues. In all groups, cells showed spontaneous contraction from day 1, and the contraction speed increased over time (Fig. 2m, Supplementary Fig. 10, and Supplementary Movie 2). The average contraction rate was significantly higher in iMPC+MN AB group, followed by iMPC AB and iMPC+MN R groups, which was consistent with the expression of MHC isoform genes (Fig. 2l). Unlike iMPC R and iMPC+MN R groups, iMPC AB and iMPC+MN AB cells contracted along the direction of the cellular arrangement (Fig. 2n, Supplementary Fig. 10b, and Supplementary Movie 3). The alignment of the cytoskeleton and laminin caused by AB (Supplementary Fig. 11) might have contributed to the directional contraction of the cells.

We evaluated the electrophysiological functions of muscle cells. A change in the intracellular calcium ion, which is related to electrophysiological and contractile functions of muscle cells⁴⁴, was measured using the fluorescent indicator of calcium ions, Fluo-4^{45–48}. The maximum intensity of Fluo-4 dye during a single cycle of calcium oscillation of the iMPC+MN AB group was higher than the values in other groups (Fig. 3a). Both the rise and decay time of the calcium oscillation were smallest in the iMPC+MN AB group. Previous studies have shown that the maximum intensity of calcium dye increased and both the rise and decay time during the contraction decreased as the muscle cells matured^{45–48}. We also observed the synchronization in the calcium intensity changes between cells, indicative of simultaneous contraction of muscle fibers⁴⁹, in the iMPC+MN AB group, unlike in iMPC+MN R group (Fig. 3b and Supplementary Movie 4). We also characterized the electric potential of cells using microelectrode array

(MEA) system⁵⁰. Compared to the iMPC R group, the iMPC+MN AB group exhibited an increased spike amplitude and reduced interspike interval in the local field potential (Supplementary Fig. 12a and b), indicating a higher electrical potential of muscle cells⁵¹. In the single unit potential recordings indicating electrical signals from neurons⁵², the iMPC+MN AB group exhibited an increase in the frequency of the signal firing (Supplementary Fig. 12c and d). These results suggest that electrophysiological functions of cells were enhanced in the iMPC+MN AB group.

To assess the functional connection between pMNs and iMPCs, we analyzed the changes in muscle contractility by the treatment of the neurotransmitter glutamate (Glut) in the region where axons from the MN can form NMJs. According to the image-based analysis, the distance between the center of MN and end of axon was similar in the iMPC+MN R and iMPC+MN AB group, with the maximum value L_{\max} of approximately 130 μm (Fig. 3c). In the overlay of the brightfield and fluorescent images of MNs, the area within L_{\max} from the motor neuron was defined as the near region, where pMN axons can form NMJs, while the area beyond L_{\max} was defined as the far region (Fig. 3d). Cellular contraction in near and far regions was characterized before and after the Glut treatment for both the iMPC+MN R and iMPC+MN AB groups (Fig. 3e). In both groups, Glut treatment induced an increase in contractility of muscle cells in the near regions, not in the far regions (Fig. 3f). Notably, the Glut-induced enhancement of contractility of muscle cells in the near regions was more significant in the iMPC+MN AB group compared to iMPC+MN R group, suggesting that co-patterning of iMPCs and MNs by AB facilitates more efficient NMJ formation. We further analyzed the excitatory response of muscle cells following treatment with neurotransmitters such as Glut and acetylcholine (ACh). Treatment with Glut, which specifically stimulates pMNs, only increased the calcium transient in both iMPC+MN R and iMPC+MN AB groups (Supplementary Fig. 13), indicating that signal transmission from pMNs to iMPCs through NMJs occurred in those groups. The injection of ACh following Glut treatment caused iMPCs to exhibit increased calcium transients with synchronous and strong contractions by activating their AChRs in all groups. The pre-treatment with 1 mM tubocurarine (TC), a blocking agent for AChRs, prevented the change of calcium transients by Glut and ACh treatment⁵³. In summary, co-patterning iMPCs and MNs in close proximity through AB can significantly enhance the opportunity for NMJ formation, leading to the generation of more functionally advanced NMJ tissue.

AB applications for regenerative medicine

We examined the therapeutic potential of tissues fabricated by the AB method in the treatment of traumatic injuries such as VML. iMPCs were generated ten days prior to tissue transplantation (Fig. 4a). 3D neuromuscular tissues were fabricated 24 h before transplantation. The tissue construct in the mold was transferred to the VML site directly in order to prevent physical damage to the tissue (Supplementary Movie 5). Mice that did not undergo VML induction or that did not receive treatment after VML induction were denoted as Normal and NT (no treatment), respectively. The mice transplanted with the cell-free hydrogel were referred to as Gel only group. The mice transplanted with cell-laden tissues were identified based on the names of the specific transplanted tissues, including iMPC+MN R, iMPC AB, and iMPC+MN AB. The recovery of host tissues by the transplantation was determined through histological and behavioral analyses up to 12 weeks. In the histological analysis, the regenerated site was defined as the region of small myofibers with centralized nuclei which are observed during muscle regeneration^{54,55} (Fig. 4b).

The early therapeutic effect of the tissues was examined by transplanting the iMPC AB tissues containing cells labeled with a fluorescent membrane dye (DiI). On day 5 after tissue transplantation, both the DiI-positive/MHC-positive cells from the transplanted tissues and DiI-negative/MHC-positive cells from the host were observed in

the regenerated region (Supplementary Fig. 14). More MHC-positive/desmin-positive muscle fibers with centralized nuclei were observed in iMPC AB group than in the NT group. This result suggests that iMPCs in the transplanted tissue survive in the host tissue, interact with the recruited host cells, and stimulate muscle fiber formation. We further analyzed the host immune response by performing immunohistochemical detection of macrophage (Supplementary Fig. 15) on day 5 after the transplantation. Immune cell infiltration was increased in the NT group compared to the Normal group. The iMPC AB group showed alleviated inflammation than the NT group, which might be attributed to rapid muscle regeneration^{56,57} by the transplanted tissue, relative to the NT group.

Masson's trichrome (MT)-stained cross-sectional images of the quadriceps femoris (QF) muscles at 6 and 12 weeks after transplantation showed significant restoration of muscle volume in iMPC+MN R, iMPC AB, and iMPC+MN AB groups (Fig. 4c). Immunofluorescence images at 6 weeks revealed that the thickness of the regenerated region was significantly larger in iMPC+MN AB group than in other groups (Supplementary Fig. 16). The enhanced differentiation of iMPCs into myofibers by co-culturing of pMNs and AB (Fig. 2i, k, and l) and the survival of differentiated myofibers at the defect site (Supplementary Fig. 14) might increase the area of the regenerated region.

The image analysis showed that the number of myofibers with centralized nuclei was highest in the iMPC+MN AB group (Fig. 4d). The fibrotic area of the collagen deposition due to inflammation progressively decreased with time and was close to zero for iMPC+MN AB group at 12 weeks (Fig. 4e). The cross-sectional area (CSA) of newly formed muscle fibers, indicative of the force generated by the skeletal muscle tissue⁵⁸, increased over time (Fig. 4f). The iMPC+MN AB group showed a higher average CSA compared to other groups except Normal group. We further compared the histograms of the CSA of groups that received treatment versus that of Normal or NT group at 12 weeks (Supplementary Fig. 17). Only for iMPC+MN AB group, the similarity of the CSA histogram versus Normal group was higher than that versus NT group (Fig. 4g).

Because vascularization and neuronal innervation in the transplanted tissue are required for the structural and functional recovery of the skeletal muscle⁵⁹, we quantified the number of blood vessels, AChRs, and NMJs through image-based analysis of immunofluorescence images (Fig. 5a and b). Compared to Normal group, NT and Gel only groups exhibited a slightly higher number of capillaries and a lower number of AChRs and NMJs (Fig. 5c, d, and e). The increased number of capillaries in those groups might be attributed to the secretion of paracrine factors during the self-regenerative process of skeletal muscle upon injury⁶⁰. Compared to NT and Gel only groups, the number of capillaries, AChRs, and NMJs increased significantly in the groups transplanted with the cell-laden hydrogel such as iMPC+MN R, iMPC AB, and iMPC+MN AB. The iMPC+MN AB group had the highest values among the three groups, indicating that the infiltration of blood vessels and motor neurons from the host tissue into the transplanted tissue was enhanced by AB.

To investigate the effect of the transplantation of neuromuscular tissues fabricated with AB on the functional recovery of mouse hind limbs with VML, we conducted *in vivo* electrophysiology assessment, hind limb grip tests, and weight bearing analysis^{61–63} (Fig. 5f–r). To verify the electrophysiological improvement of the skeletal muscle *in vivo*, we evaluated the forces generated by the muscle tissues in response to electrical stimuli (Fig. 5f). The single and multiple pulsed electrical stimuli were applied to the tissues to evaluate their twitch and tetanic contractile properties, respectively (Fig. 5g, h). The relative twitch and tetanic forces compared to their pre-operative (Pre-op) values showed a continuous increase from 2 weeks to 6 weeks in all groups (Fig. 5i and j). At 6 weeks, both the relative twitch and tetanic force of the iMPC+MN AB group were significantly higher than those of the NT group. The relative twitch force of the iMPC+MN AB group at

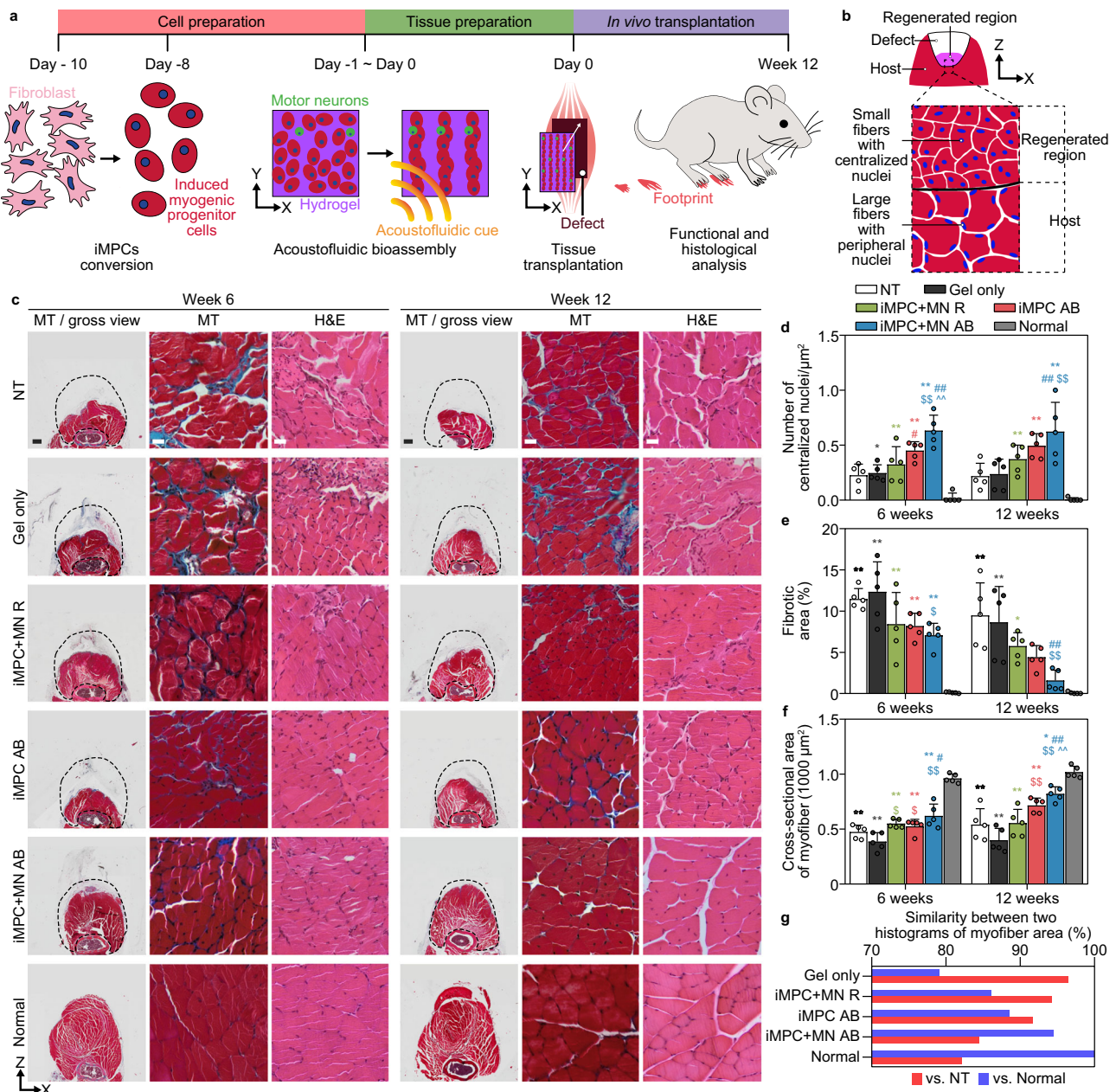


Fig. 4 | Transplantation of neuromuscular tissues fabricated by acoustofluidic bioassembly method for volumetric muscle loss. **a** Schematic diagram and timeline of production and implantation of 3D neuromuscular tissue generated by acoustofluidic bioassembly (AB). **b** Schematic of muscle fibers in the defect, regenerated region, and host region in the cross-section of skeletal muscle. In normal skeletal muscle (host), the nuclei of muscle fibers are located at the periphery of the muscle fiber. Myofibers with central nuclei are observed in the regenerated region. **c** Representative images of Masson's trichrome (MT) and Hematoxylin and eosin (H&E) stained cross-sections of volumetric muscle loss (VML)-injured quadriceps muscles at 6 and 12 weeks after. Black dotted lines in gross view represent the host regions before ablation. Scale bars in gross view and

microscopic image represent 500 μm and 20 μm , respectively. **d-f** Quantitative analysis of the number of centralized nuclei (**d**), fibrotic area (**e**), and the average cross-sectional area (CSA) of myofiber (**f**) based on MT staining images ($n = 5$ biologically independent samples). **g** Similarity of the histograms of CSA of myofibers of gel only, iMPC+MN R, iMPC AB, or iMPC+MN AB groups versus (vs.) those of NT or normal groups. All data are presented as mean \pm S.D., and statistical differences were determined with one-way ANOVA followed by Tukey's test. # $P < 0.05$ and ## $P < 0.01$ versus NT, \$ $P < 0.05$ and \$\$ $P < 0.01$ versus gel, ^ $P < 0.01$ versus iMPC+MN R, and * $P < 0.05$ and ** $P < 0.01$ versus Normal. Source data are provided as a Source Data file.

6 weeks approached that of the Normal group. The maximum rate of contraction and relaxation in all groups increased from 2 weeks to 6 weeks (Fig. 5k and l). The maximum rates in the iMPC+MN AB group at 6 weeks reached a level between the Normal and NT groups. We evaluated the resistance of the muscle against the fatigue by analyzing the characteristic time it took for the force to reach 50% of its initial value under the continuous electrical stimulation (Fig. 5m). In the iMPC+MN AB group, the characteristic time was shorter than that in the

Normal group but longer than that in the NT group (Fig. 5n). The weight bearing assay, which evaluates the balance of the weight support between Normal and impaired hindlimbs (Fig. 5o), showed that there was a significant imbalance in the NT group at 6 weeks, unlike the Normal group (Fig. 5p). The weight distribution in the iMPC+MN AB group was more balanced compared to the NT group. We further measured the grip strength of injured hindlimbs (Fig. 5q). As the mouse grew, the grip strengths of Normal, iMPC+MN R, iMPC AB, and

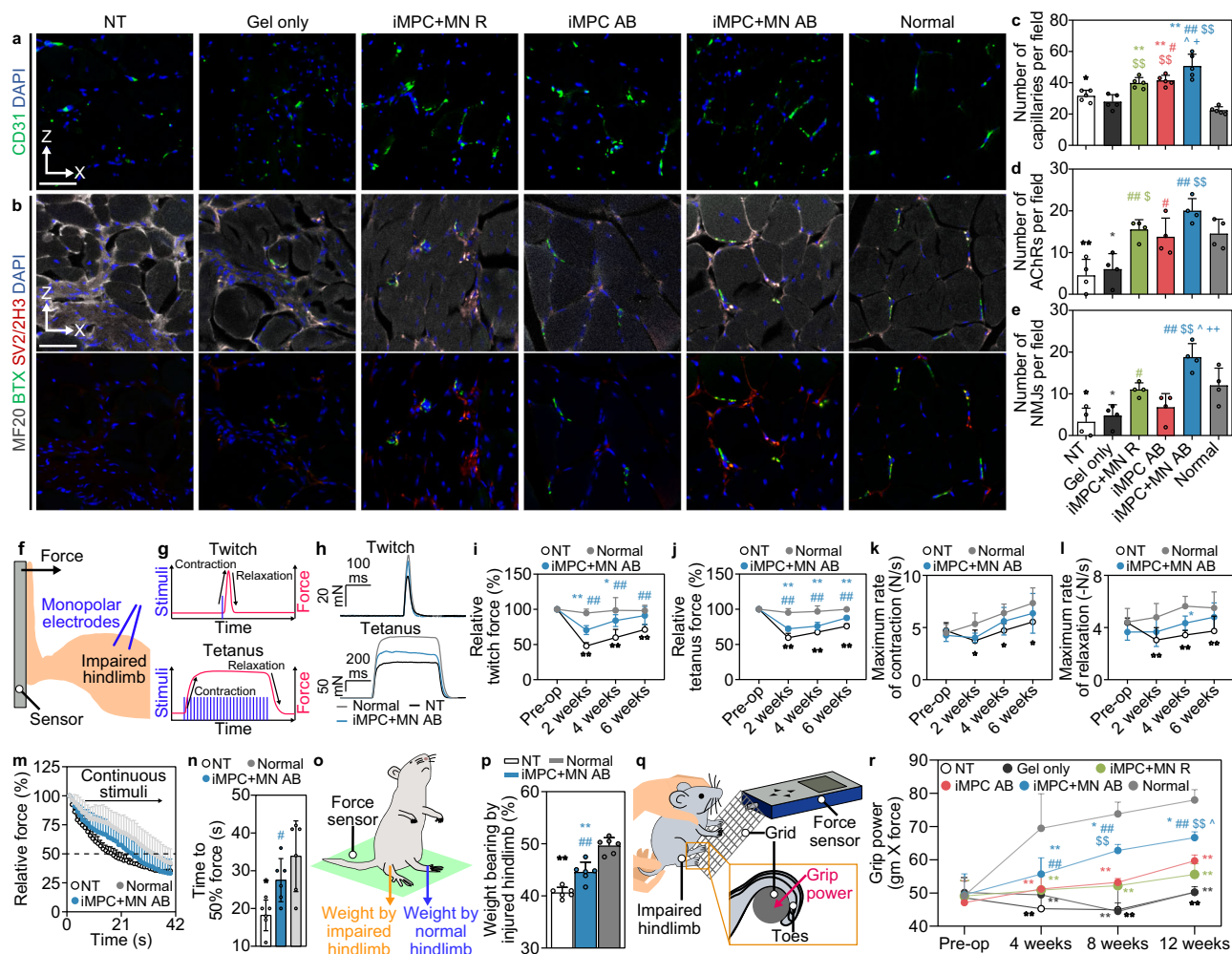


Fig. 5 | Functional restoration using transplanted tissues formed with acoustic-tofluidic bioassembly. a, b Immunostaining images of CD31 (green) and DAPI (blue) (a) and MF20 (gray), BTX (green), SV2/2H3 (red), and DAPI (blue) (b) of injured muscles at 12 weeks. The bottom rows in (b) are the merged images without MF20. Scale bars represent 50 μ m. **c–e** Number of capillaries (c) ($n=5$), AChRs (d) ($n=4$), and NMJs (e) ($n=4$) per field. **f** Schematic of the force measurement of the impaired muscle using electrical stimuli from electrodes. **g–h** Schematic of the force (red) made by electrical stimuli (blue) (g) and representative force plots during the twitch and tetanic behavior (h). **i–l** Twitch (i) and tetanic (j) force, maximum rate of contraction (k) and relaxation (l) at pre-operation (Pre-op) and 2, 4, and 6 weeks ($n=6$ biologically independent samples). The forces were normalized by values at Pre-op. **m, n** Force decay during tetanic stimulation (m) and time required to reach 50% of the initial values (n) at 6 weeks ($n=6$ biologically independent samples). **o** Schematic of the weight-bearing analysis. **p** Weight bearing

ratio of the injured to the uninjured hindlimb in the NT, iMPC+MN AB, and Normal groups at 6 weeks ($n=6$ biologically independent samples). **q** Schematic of the grip strength test. **r** Grip strength at Pre-op and 4, 8, and 12 weeks ($n=9$ biologically independent samples for NT, gel, and Normal, and $n=10$ biologically independent samples for other groups at Pre-op and 4 weeks; $n=4$ biologically independent samples for NT, gel, iMPC+MN R, and iMPC+MN AB and $n=5$ biologically independent samples for other groups at 8 and 12 weeks). All data are presented as mean \pm S.D. Statistical differences in (c), (d), (e), (n) and (p) were determined with a one-way ANOVA followed by Tukey's test, and those in (i), (j), (k), (l), and (r) were determined with a two-way ANOVA followed by Tukey's test. # $P<0.05$ and ### $P<0.01$ versus NT, \$ $P<0.05$ and \$\$\$ $P<0.01$ versus gel, * $P<0.05$ versus iMPC+MN R, + $P<0.05$ and ++ $P<0.01$ versus iMPC AB, and * $P<0.05$ and ** $P<0.01$ versus Normal. Source data are provided as a Source Data file.

iMPC+MN AB groups continuously increased (Fig. 5r). The iMPC+MN AB group exhibited the most significant improvement in grip strength throughout the 12-week recovery process.

The behavioral characteristics of the mouse were evaluated by open field test, rotarod assay, and gait analysis^{62,64}. From the open field test which analyzes the track of motion of mouse in the square-shaped box using the video camera (Fig. 6a and b), the locomotive performance, represented by the total traveled distance and the percentage of mobile time, was significantly decreased in the NT group at 6 weeks (Fig. 6c and d). The mobility of the iMPC+MN AB group was similar to that of the Normal group. We further measured the latency to fall of the mouse from a rotating rod with accelerated rotational speed (Fig. 6e). At 2, 4, and 6 weeks, the latency time of the NT group was significantly shorter than that of the Normal group (Fig. 6f). The

latency duration of the iMPC+MN AB group was longer than that of the NT group at 2, 4, and 6 weeks and approached that of the Normal group at 6 weeks. We also assessed the mobility through gait behavior analysis (Fig. 6g and Supplementary Fig. 18a). Four weeks after transplantation, in Normal group, the stride length was increased by the growth of mouse (Fig. 6h and Supplementary Fig. 18b). All injured groups exhibited abnormal gait behavior, indicated by shorter stride length and increased sway length compared to their Pre-op values and that of the Normal group (Fig. 6h and i and Supplementary Fig. 18). The enhancement of gait behavior over time, indicated by increased stride length and decreased sway length, was significant in iMPC AB, iMPC+MN R, and iMPC+MN AB groups compared to NT and Gel only groups. The iMPC+MN AB group exhibited stride and sway lengths comparable to those of Normal group. The enhanced functional restoration of the

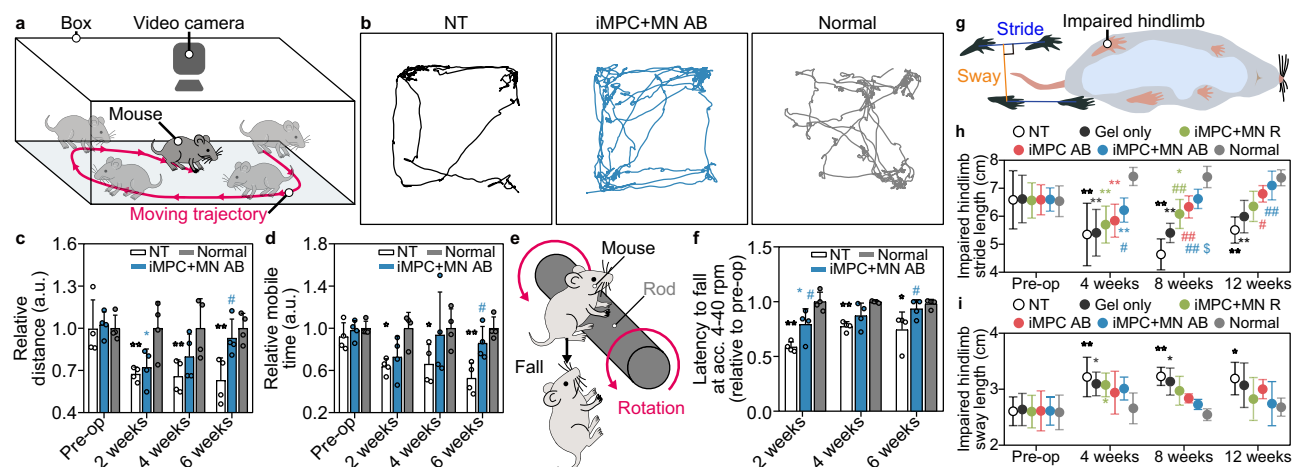


Fig. 6 | Behavioral restoration with transplanted tissues formed with acoustofluidic bioassembly. **a** Schematic of open field analysis. **b** Representative plots of the moving trajectories of the mice at 6 weeks in the open field tests. **c–d** Relative distance (**c**) and relative mobile time (**d**) of the mice at pre-operation (Pre-op), 2, 4, and 6 weeks ($n = 4$). **e** Schematic of rotarod assay. **f** Latency to fall at acceleration (acc.) from 4 to 40 rpm of the mice at 2, 4, and 6 weeks normalized to values at Pre-op obtained from the rotarod assay ($n = 4$). **g** Schematic illustration of quantification of sway and stride in the gait analysis for the hindlimbs. **h–i** Measurements of

injured hindlimb stride length (**h**) and sway length (**i**) at Pre-op, 4, 8, and 12 weeks post-implantation with 3D fabricated neuromuscular tissues ($n = 9$ biologically independent samples for Normal and $n = 10$ biologically independent samples for all other groups at Pre-op and 4 weeks; $n = 5$ biologically independent samples at 8 and 12 weeks). a.u., arbitrary units. All data are presented as mean \pm S.D. Statistical differences were determined with a two-way ANOVA followed by Tukey's test. $\#P < 0.05$ and $\#\#P < 0.01$ versus NT, $\$P < 0.05$ versus gel, and $*P < 0.05$ and $**P < 0.01$ versus Normal. Source data are provided as a Source Data file.

defective hind limb might be caused by an increase in the CSA of myofibers and upregulation of AChR and NMJ formation by AB.

Discussion

In situ fabrication of tissues is emerging as one of the promising strategies in regenerative medicine due to its applicability for various clinical situations^{65,66}. We applied the AB method to fabricate an in situ tissue construct with in vivo-like cellular arrangement at the site of tissue defect. The portable acoustofluidic device was loaded onto the defect site in hind limb skeletal muscle of a living mouse (Fig. 7a–c). After injection of the hydrogel solution containing iMPCs into the defect area, acoustofluidic cues were applied to induce the arrangement of cells into 3D parallel cylinders in the hydrogel construct on the living muscle tissue (Fig. 7d and e). In the histological image at 5 days post-transplantation, we could observe that an organized alignment consistent with the native muscle structure (Supplementary Fig. 19), providing direct visual evidence of the tissue repair achieved by the in situ-engineered constructs. We further explored the applicability of the AB method in the regeneration of a disconnected spinal cord (Fig. 7f and g). We fabricated neural tissues at the defect site using human induced pluripotent stem cell (hiPSC)-derived neural progenitor cells (hiPSC-NPCs), which were utilized in clinical trials for spinal cord injury⁶⁷. The acoustofluidic device was loaded into the dissected area of the ex vivo spinal cord isolated from mouse. After injecting a hydrogel solution with hiPSC-NPCs into the dissected region, acoustofluidic cues were applied to form the tissue constructs that replicated the cell alignment observed in the spinal cord. The hiPSC-NPCs in the tissue fabricated using the AB method exhibited axonal sprouting aligned parallel to the major axis of the spinal cord, which was compared to the isotropic sprouting observed in the tissue prepared from the cell-hydrogel mixture (Fig. 7g). The proper alignment of neural cells is beneficial to enhance the regeneration of damaged nerve fibers. These in situ applications demonstrate the potential of AB as a tool for constructing tissues in an intraoperative manner^{65,68}. Our tissue fabrication device could be developed as a benchtop or handheld form (Fig. 7h).

We used the direct cell conversion technique, which refers to the conversion of one type of somatic cells into another type without

bypassing the pluripotent state, allowing the rapid production of therapeutic cells for treating acute conditions like VML from war or traffic accidents⁶⁹. However, there are debates regarding their limitations, including low efficiency and unstable functionality of the converted cells⁷⁰. Additionally, the extraction of primary cells from tissue through biopsy can cause significant pain and permanent damage to the patient⁷¹. For this reason, we further assessed the applicability of our method for tissue fabrication using hiPSC-derived cells, which exhibit good quality and resemblance to in vivo cells⁷². The hiPSC-MPCs and hiPSC-MNs, which were differentiated from hiPSCs using the protocols in previous studies^{73–76} (Fig. 8a), expressed specific markers for each types of cell (Fig. 8b, c). The hiPSC-MPC + MN R and hiPSC-MPC + MN AB groups were viable during 5 days of culture (Fig. 8d). Cells in the hiPSC-MPC + MN AB group exhibited an aligned structure (Fig. 8e) and showed an increased alignment index of the cytoskeleton (Fig. 8f). Our results indicate the potential of the AB method in the construction of therapeutic tissues using autologous cells.

The AB method can directly improve not only cell-cell but cell-organoid interactions. For example, the AB method increased the formation of gap junctions, induced the cytoskeleton alignment, and enhanced the contractile functions in cardiomyocytes (Supplementary Fig. 20). Also, our previous study demonstrated that the AB method enhanced the expression of tight junction in endothelial cells (ECs)³¹. The AB method could enhance the lumen formation in ECs which is mediated by direct cell-cell contact, and connect the aligned ECs with cardiac organoids (Supplementary Fig. 21). The co-arrangement of multiple cell types would help the construction of tissues innervated with vascular and neuronal networks (Supplementary Fig. 22).

Compared to state-of-the-art tissue fabrication techniques, the AB method is advantageous in terms of cell density, spatial printing resolution, versatility, and in situ applications. Physical forces that are locally focused at the nodes of the acoustic pressure field cause aggregation of cells at a high density, which is essential for tissue development^{77,78} but is difficult in conventional extrusion bioprinting methods. In the AB method, in which cell patterns are determined by those of the IDT pattern, the spatial resolution can be reduced to a dimension comparable to a single cell⁷⁹. The AB is a volumetric technique, where printing occurs simultaneously rather than sequentially.

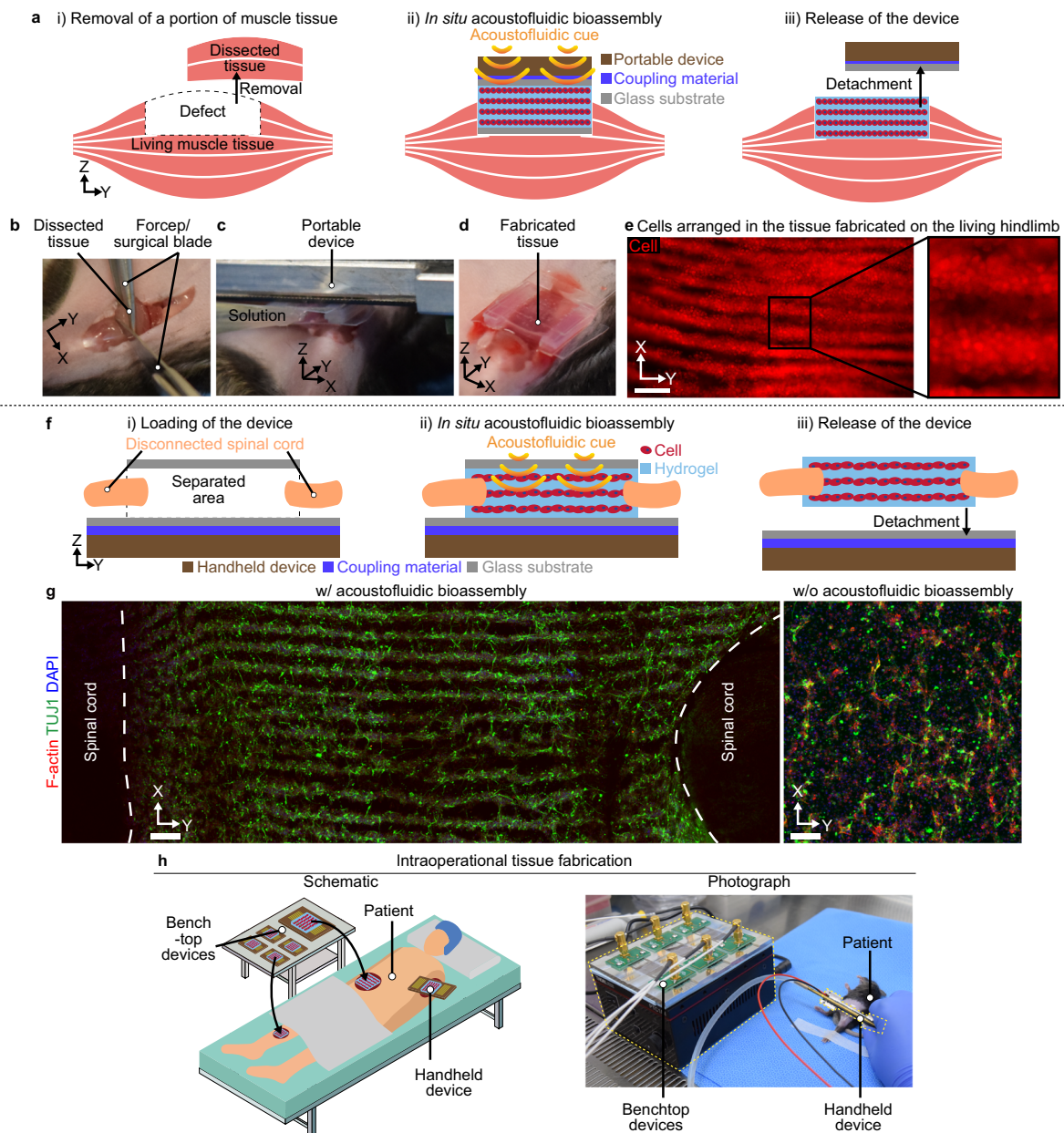


Fig. 7 | In situ acoustofluidic bioassembly. **a–e** In situ applications of acoustofluidic bioassembly for muscle regeneration. **(a)** Schematic of the in situ acoustofluidic bioassembly for tissue fabrication on live skeletal muscle tissue with volumetric muscle loss. **(b–d)** Photographs of volumetric muscle loss induced by dissecting a portion of muscle tissue of the quadriceps femoris with forceps and surgical blades **(b)**, portable acoustofluidic device loaded on the target site and injection of the cell-hydrogel solution to the target location **(c)**, and muscle tissue fabricated on the defect site of the mouse hindlimb **(d)**. **(e)** Fluorescent images of the cells (red) arranged into three-dimensional and parallel cylinders in the tissue fabricated on live muscle. Scale bar represents 200 μm . **f, g** In situ application of

acoustofluidic bioassembly for regeneration of disconnected spinal cord.

f Schematic of the in situ acoustofluidic bioassembly for tissue fabrication between the disconnected spinal cord. **g** Immunostaining images of F-actin (red)/TUJ1 (green)/DAPI (blue) of human induced pluripotent stem cell-derived neural progenitor cells (hiPSC-NPCs) in the tissues fabricated with (w/) and without (w/o) acoustofluidic bioassembly on day 5. The tissues were fabricated between the disconnected ex vivo spinal cords. White dotted lines represent the boundaries of the spinal cord tissues. Scale bars represent 100 μm . **h** Photograph and schematic of the benchtop array of devices placed near the patient and a handheld device placed on the patient inside the clean bench.

Therefore, the geometric shape and pattern of the printed cells would be less affected by the subsequent printing steps preserving printing resolution. The AB method can be further improved to replicate the heterogeneous cellular distribution with complex geometry in living tissues when combined with advanced acoustic techniques such as acoustic differential bioassembly⁸⁰, Fourier-synthesized harmonic waves⁷⁷, acoustic holograms⁸¹, or the phase-modulation technique⁸². Since the acoustic forces are generated by the contrast in acoustic properties between the printing objects and the ink, the AB method

does not require pre-treatments for objects such as labeling and coating^{30,83}. This method is versatile, and it can be applied to manipulate objects in various shapes^{84,85} or types of hydrogel material (Supplementary Fig. 23). Therefore, the AB method enables the simultaneous printing of cells with ECM proteins or nanoparticles in a label-free manner (Fig. 1f and g), which is technically challenging in conventional printing methods. The AB method in combination with current techniques^{86–88}, such as layer-by-layer stacking^{89,90} (Supplementary Fig. 24) or continuous extrusion⁹¹, will be developed into a

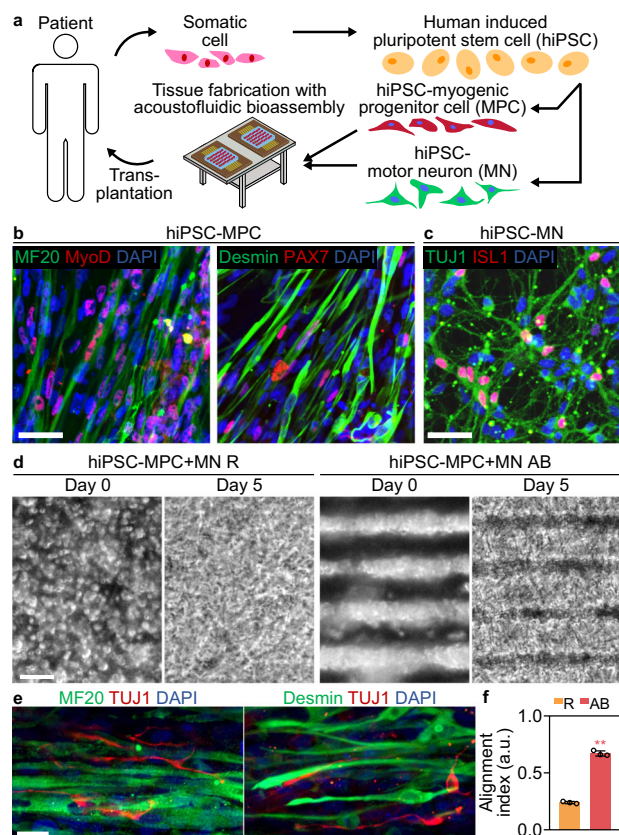


Fig. 8 | Construction of the neuromuscular tissues using human induced pluripotent stem cell (hiPSC)-derived myogenic progenitor cells (MPCs) and motor neurons (MNs). **a** Schematic of strategies in personalized tissue fabrication with acoustofluidic bioassembly using hiPSC-derived MPCs and MNs. **b** Immunofluorescence images of hiPSC-derived MPCs after differentiation, stained with MF20 (green)/MyoD (red)/DAPI (blue) and Desmin (green)/PAX7 (red)/DAPI (blue). **c** Immunofluorescence image of TUJ1 (green)/ISL1 (red)/DAPI (blue) of hiPSC-derived MNs after differentiation. **d** Brightfield images of the neuromuscular tissues of hiPSC-MPC + MN R and hiPSC-MPC + MN AB groups at day 0 and 5. **e** Immunofluorescence images of the tissues of the hiPSC-MPC + MN AB groups at day 5 stained with MF20 (green)/TUJ1 (red)/DAPI (blue) and desmin (green)/TUJ1 (red)/DAPI (blue). **f** Alignment index of the cells in the hiPSC-MPC + MN R (R) and hiPSC-MPC + MN AB (AB) groups at day 5 ($n = 3$ biologically independent samples; $**P < 0.01$ versus R). a.u., arbitrary units. Scale bars in (b–e) represent 50 μm , 100 μm , and 25 μm , respectively. Data is presented as mean \pm S.D., and statistical differences were determined with an unpaired, two-sided t-test. Source data are provided as a Source Data file.

complementary platform for fabricating 3D tissue constructs that replicate the structure and function of in vivo organs at scales. Still, our method has technical limitations in simulating the spatial gradient in the composition of tissues and alternating arrangement of different types of cells which are found in biological tissues. These would be overcome by integrating our device with a microfluidic mixer⁹² or by regulating acoustic properties of cells via genetic modifications⁹³.

Previous studies have shown the capability of acoustic bioassembly techniques using bulk acoustic wave and Faraday wave devices to fabricate large-scale tissues with homocellular and heterocellular interactions^{80,94,95}. In this study, utilizing a SAW-based device, we demonstrated (1) the therapeutic efficacy of acoustofluidic bioassembled neuromuscular tissues and (2) the in situ formation of tissues via acoustofluidic bioassembly—achievements that had not been reported in the previous studies^{80,94,95}.

Various tissue fabrication techniques, such as organoid and 3D bioprinting, have been utilized to investigate cell-cell and cell-ECM interactions. Organoids, which can effectively mimic in vivo organs and

tissues, face challenges in controlling the geometric arrangement of cell components. The nozzle-based 3D bioprinting of cells has advantages in controlling cellular arrangement. However, it is limited in promoting cell-cell contacts due to the printable cell density. Our technology can be advantageous in controlling the geometric patterns of cellular aggregates and microstructure of surrounding ECM at a high resolution.

In summary, the acoustofluidic bioassembly induced morphogenesis enables the rapid fabrication of clinically-relevant-sized tissues with structures engineered at nano/micro/macro scales. The AB method enables the creation of neuromuscular tissues that are highly functional and have high therapeutic efficacy against injuries such as VML. We further demonstrated the application of the AB method for the in situ fabrication of tissues at desired locations to replace defective tissues. We believe that acoustofluidic bioassembly induced morphogenesis holds potential for creating in vitro tissues for applications including regenerative medicine and drug screening.

Methods

Piezoelectric device fabrication

Interdigital transducers were deposited onto a piezoelectric material of 128° Y-cut lithium niobate (LiNbO₃) using the photolithography technique^{31,96,97}. Briefly, the device was fabricated in the following processes. Aluminium was sequentially deposited on the wafer. The thickness of the aluminium layer was 20000 Å. Photoresist was spin-coated on the LiNbO₃ substrate. After the alignment of photomask, the UV light was illuminated on the photoresist. After the removing the UV-illuminated photoresist by treating with developer solution, the aluminium layer was wet etched. The remaining photoresist was removed by treating with the remover solution. The aluminium-patterned LiNbO₃ wafer was diced into desired shapes. After depositing the conductive epoxy glue on the aluminium die, the piezoelectric device was placed on the top of the epoxy and the epoxy was cured at 80 °C for 3 hours. A silicone thermal pad was attached to the bottom of the aluminium die, which was then placed onto the Peltier-based temperature control system. The electrode pads for the IDT were connected to pogo pins integrated with the printed circuit board (PCB). The PCB and aluminum die were also secured together using bolts. The surface of the PCBs was sealed with epoxy. IDTs were connected to an RF amplifier (LZY-22+, Mini-Circuits) and a function generator (33622 A, Keysight, Santa Rosa, CA, USA). The distance between the neighboring electrodes in IDTs of the device for the in vitro and in vivo experiments and the IDT width were 70 μm , and the frequency of the RF signal applied to these IDTs was approximately 14 MHz.

The interval between the pattern of cells, which is a key parameter of the morphological characteristics of the tissues, was linearly proportional to the distance between the electrode geometry (Supplementary Fig. 25a). The percentage of cells with neighbors, which may influence the maturation and expression of key functions of cells, is reduced when the interval between the cell patterns decreases at a consistent cell density (Supplementary Fig. 25b).

Preparation of tissue mold

In this study, we regulated the height of the gel solution and coupling liquid to be 400 μm and 100 μm , respectively, by cutting the rubber structure and spacer from rubber film products (Elastosil 2030, Wacker, Munich, Germany) (Supplementary Fig. 26) using a cutting device (CE6000-120, Graphtec, Yokohama, Japan)^{98–100}.

The mold for the tissue was prepared by assembling a glass cover, rubber structure, and glass substrate. The assembled mold was sterilized with the 70% v/v (volume/volume) ethyl alcohol solution and UV (ultraviolet) light for over 30 min and washed with a 1X phosphate-buffered saline (PBS) solution three times. Rubber spacers were positioned on the piezoelectric device to hold the mold. The coupling liquid, 1X PBS solution, was injected into the space between the mold and the piezoelectric device.

Numerical analysis of acoustic fields in the acoustofluidic device
A finite element method (FEM) was employed to simulate acoustic fields in an acoustofluidic device using COMSOL Multiphysics software (COMSOL, Stockholm, Sweden)³¹. The FEM analysis was conducted in the frequency domain.

The ‘Piezoelectric Devices’ module, which couples the ‘Solid Mechanics’ and ‘Electrostatics’ modules, was used to develop a model for the domain of piezoelectric material. ‘Pressure Acoustic’ and ‘Thermoviscous Acoustic’ modules were used to develop a model for the coupling liquid and hydrogel solution domains, respectively. For the PDMS rubber domain, the ‘Pressure Acoustics’ module was applied assuming the shear wave was negligible in the PDMS rubber¹⁰¹. The domains for the bottom and top glass substrates and glass mold were modeled using a ‘Solid Mechanics’ module. The ‘Thermoviscous-Acoustic Structure Boundary’ condition was applied to the interface between the glass and gel solution. The ‘Acoustic-Thermoviscous Acoustic Boundary’ condition was applied to the interface between the mold and the gel solution. The ‘Acoustic-Structure Boundary’ was applied to the interfaces between domains to which the ‘Pressure Acoustics’ and ‘Solid Mechanics’ modules were used. The detail mathematical description and the material properties of the FEM model were described in the Supplementary Note 7.

Cell isolation and culture

Primary mouse embryonic fibroblasts (pMEFs) were isolated from ICR mouse embryos (Orientbio, Seongnam, Korea) on embryonic day 13.5 (E13.5) as previously described¹⁰². The head, limbs, spinal cord, and internal organs were removed, and the remaining tissues were digested in DNase I solution (Takara Bio Inc., Shiga, Japan) for 10 min at 37°C. The isolated cells were cultured on 0.2% gelatin (Sigma-Aldrich, St. Louis, MI, USA)-coated substrate in Dulbecco’s modified Eagle’s medium (DMEM; Thermo Fisher Scientific, Waltham, MA, USA) supplemented with 10% (v/v) fetal bovine serum (FBS, Thermo Fisher Scientific), 1% (v/v) non-essential amino acids (NEAA, Thermo Fisher Scientific), 1% (v/v) penicillin/streptomycin (PS, Thermo Fisher Scientific), and 0.1% β -mercaptoethanol (Thermo Fisher Scientific) for 2–3 days at 37°C in a 5% CO₂ atmosphere. pMEFs at passages 1–2 were used for successful reprogramming.

Primary mouse motor neurons (pMNs) were isolated from ICR mouse embryos (Orientbio) on embryonic days 13.5–14.5 (E13.4–14.5). The isolation of pMNs from the embryo’s spinal cord was performed as previously described, with some modifications^{103,104}. To purify the motor neurons from the embryonic spinal cord, a 10 cm culture dish (Corning, NY, USA) was coated with 10 μ g/mL lectin (Sigma-Aldrich) dissolved in 10 mM Tris (Biosesang, Seongnam, Korea) at pH 9.5. The spinal cord was separated from the embryo, and the meninges were detached from the dorsal root ganglia and washed with Hanks’ Balanced Salt Solution (HBSS, Thermo Fisher Scientific). The lumbar portions of the spinal cord were digested with 0.5% Trypsin-EDTA (0.1%, final; Thermo Fisher Scientific) for 15 min at 37°C. Trypsinization was stopped by adding trypsin inhibitor (0.1%, final; Sigma-Aldrich). Cell aggregates were gently triturated using a pipette and transferred to a pre-coated lectin dish in HBSS at room temperature for 1 h. Following the incubation period, the dish was washed carefully three times with pre-warmed HBSS to remove cell fragments and unattached cells. Next, 30 mM KCl (Sigma-Aldrich), 0.8% (w/v) NaCl (Sigma-Aldrich) depolarization solutions were added to the plate and incubated for 1 min. The detached cells were collected in neurobasal medium (Thermo Fisher Scientific) and used for subsequent experiments.

Generation of induced muscle progenitor cells (iMPCs)

pMEFs were transfected with plasmids encoding the genes *Mef2c*, *MyoD*, *Pax7*, and *Pitx1* (Origene, Rockville, MD, USA) using electroporation (4.5 μ g each gene per 10⁶ cells, Neon, Thermo Fisher

Scientific). The electroporated cells were plated on Matrigel (Corning)-coated culture plates with DMEM (Thermo Fisher Scientific) supplemented with 10% FBS (Thermo Fisher Scientific), 1% NEAA (Thermo Fisher Scientific), and 0.1% β -mercaptoethanol (Thermo Fisher Scientific) at a density of 2 × 10⁴ cells per cm² growth area. After 2 days, the electroporated cells were re-transfected with 0.35 μ L Lipofectamine 2000 (Thermo Fisher Scientific) per 0.35 μ g of each plasmid DNA per cm². Four hours after transfection, the DMEM was replaced with myogenic induction medium containing DMEM/F-12 (Thermo Fisher Scientific) supplemented with 10% FBS, 10% (v/v) Knock-out Serum replacement (Thermo Fisher Scientific), 1% (v/v) NEAA, 1% PS, 0.1% β -mercaptoethanol, 10 ng/mL basic fibroblast growth factor (Peprotech, Rocky Hill, NJ), 5 μ M Forskolin (LC Laboratory, Woburn, MA, USA), 3 μ M CHIR99021 (LC Laboratory), and 5 μ M Repsox (Sigma-Aldrich)¹⁰⁵. The myogenic induction medium was replaced every alternate day, and contracting iMPCs were observed within a week of the first transfection.

Three-dimensional aligned neuromuscular tissue construct

The hydrogel mixture was prepared following the previous study⁴¹, with some modifications. The hydrogel solution was prepared by dissolving bovine fibrinogen (Sigma-Aldrich) in Dulbecco Phosphate Buffered Saline (DPBS, Sigma-Aldrich) and supplemented with growth factor-reduced Matrigel (Corning). The fibrin hydrogel was chosen because it is more amenable to muscle cell contraction than other matrix proteins^{42,106} and can be rapidly cross-linked¹⁰⁷. Cells were then injected into the mixture of fibrinogen and Matrigel. Pre-gel solutions containing cells were mixed with thrombin (Sigma-Aldrich) and immediately transferred into the tissue mold in the piezoelectric device. The density of iMPCs was 1 × 10⁷ cells/mL. For the construction of tissues for iMPC+MN R and iMPC+MN AB groups, pMNs were added to the iMPCs-laden pre-gel solution. The iMPCs:pMNs ratio was optimized at 200:1 based on the number of MF20 (myosin heavy chain; MHC)-positive cells in the two-dimensional culture (Supplementary Note 5). The final concentrations of fibrinogen, Matrigel, and thrombin were 4 mg/mL, 20% v/v, and 8 U/mL, respectively.

Acoustofluidic cues were applied to the hydrogel solution by exerting sinusoidal electrical signals on IDTs for 2 min during the solidification of fibrin gel. The temperature of the hydrogel-containing cells was maintained below 36°C using a cooling system. After gelation of the fibrin, the tissue mold was detached from the device and incubated further at 37°C for 20 min for the polymerization of Matrigel. The cell-laden hydrogel was then transferred to a culture dish and immersed in myogenic induction medium supplemented with 2 mg/mL 6-aminocaproic acid (Sigma-Aldrich). The 3D muscle constructs were cultured until the given day of the experiment with the medium being changed on alternate days.

For the arrangement of cells into curved patterns, the IDTs were designed to have a shape of intertwined spiraling lines^{108,109} and deposited on an X-cut LiNbO₃ substrate. The PBS solution containing cells was injected between the IDTs and the coverglass which were separated by a 100 μ m thick rubber spacer.

For the fabrication of the large-sized tissue, cells were mixed with the solution of methacrylated gelatin (GelMA; Allevi, Philadelphia, PA, USA) hydrogel containing photoinitiator of 2-hydroxy-4’-(2-hydroxyethoxy)-2-methylpropiophenone (Irgacure 2959; BASF Schweiz, Kaisten, Switzerland). The pre-gel solution was heated to 37°C and transferred into the mold followed by the application of the acoustofluidic cues for 3 min. The hydrogel was solidified by the irradiation of the UV light for 2 min. The photocuring intensity and the corresponding power density was 5 mWcm⁻² and 600 mJcm⁻². The density of cells was 1 × 10⁷ cells/mL. The final concentrations of the GelMA and photoinitiator were 5% and 0.1%, respectively. The density of cells was 1 × 10⁷ cells/mL. The final concentrations of the GelMA and photoinitiator were 5% and 0.1%, respectively.

Cell viability assay

Cell viability was assessed using a LIVE/DEAD Viability/Cytotoxicity assay kit (Thermo Fisher Scientific) according to the manufacturer's instructions. 3D muscle constructs were incubated in DPBS containing 2 μ M calcein-acetoxymethyl (Thermo Fisher Scientific) and 4 μ M ethidium homodimer-1 (Thermo Fisher Scientific) at 37 °C for 30 min. After washing with DPBS, live and dead cells were visualized using a confocal laser-scanning microscope (LSM 880, Carl Zeiss, Oberkochen, Germany). The numbers of live cells (green) and dead cells (red) were counted manually, and the percentage of viable cells was calculated ($n = 3$) using the confocal images.

Immunocytochemistry

Cells cultured on 2D substrates were fixed in 10% formaldehyde for 10 min at room temperature, and 3D muscle constructs were fixed in 10% formaldehyde for 3 hours at 4 °C while rocking. Before staining, samples were permeabilized and blocked in phosphate-buffered saline (PBS; Biosesang, Seongnam, Korea) containing 10% FBS, 1% (w/v) bovine serum albumin (BSA; MP Biomedicals, LLC, Santa Ana, CA, USA), and 0.5% (v/v) Triton-X 100 (Sigma-Aldrich). The samples were then incubated with primary antibodies overnight at 4 °C (Supplementary Table 1).

Image-based quantification

The myofiber diameter was obtained by manually measuring the thickness perpendicular to the longitudinal direction of the myofibers in 3D neuromuscular tissues. The percentage of MyoG-positive nuclei was calculated by dividing the number of MyoG-positive nuclei by the total number of nuclei. The fusion index was calculated by dividing the number of nuclei in the multinucleated myofibers by the total number of nuclei in the image field. The striated myofiber density was calculated by dividing the number of striated myofibers by the total number of myofibers. The number of AChRs visualized by BTX staining was counted manually. Neuromuscular junctions were defined as sites where BTX+ AChRs on the MF+ myotubes and SV2/2H3+ neurofilaments colocalized. The number of NMJ was quantified manually. For all image quantification analyses, at least three random fields of view were analyzed per group for each of the two or three independent experiments using the image analysis software Fiji¹⁰ (National Institutes of Health, Bethesda, MD, USA).

Quantitative real-time polymerase chain reaction (qPCR)

Total mRNA was extracted from each sample using an RNA extraction kit (Takara Bio Inc., Shiga, Japan), and cDNA was synthesized from the mRNA using the PrimeScript II First Strand cDNA Synthesis Kit (Takara Bio Inc.). qPCR was performed with the synthesized cDNA using the TaqMan Fast Universal Master Mix (Thermo Fisher Scientific) and the StepOnePlus Real-Time PCR System (Thermo Fisher Scientific). Gene expression was quantified using TaqMan Gene Expression Assays (Thermo Fisher Scientific) for each target (Pax7: Mm01354484_m1, Myf5: Mm00435125_m1, Myod1: Mm00440387_m1, Myog: Mm00446194_m1, Myh3: Mm01332463_m1, Myh8: Mm01329494_m1, Myh1: Mm01332489_m1, Myh7: Mm00600555_m1). Target gene expression was determined using the comparative C_t method, and the expression level was normalized to that of glyceraldehyde 3-phosphate dehydrogenase (GAPDH; Mm99999915_g1) as an endogenous control.

In vitro functional analyses of 3D neuromuscular tissue constructs

To investigate the contraction function of 3D neuromuscular tissue constructs, the time-lapse images of cells were obtained at 37 °C and 5 % CO₂ using a stage top incubator system (Live Cell Instrument, Republic of Korea)¹¹ on the inverted microscope (Ti-U, Nikon, Japan) equipped with a charge-coupled device (CCD) camera (DS-Q1Mc,

Nikon). The velocity of the spontaneous contraction of cells in the images was quantified from the particle image velocimetry (PIV) using an open-source software PIVlab V1.41¹² built in MATLAB R2017b (Mathworks, Natick, MA, USA).

To analyze calcium kinetics, cells were stained with 5 μ M Fluo-4 AM (Invitrogen) and 0.04% (w/v) Pluronic F-127 (Sigma-Aldrich) in myogenic induction medium for 40 min at 37 °C followed by the washing with the culture medium. Fluorescent images of Fluo-4 AM dyes were captured at 200 frames per second with a high-speed camera (C320, Vision Research, USA). The response to glutamate and acetylcholine stimulation was analyzed from the images obtained at 10 frames per second with a complementary metal-oxide-semiconductor camera (DS-Qi2). The average intensity in each region of interest (ROI) inside a cell was obtained using the image-analysis program Fiji¹⁰.

The calcium transients were investigated in terms of the peak amplitude and rise and decay time of the average calcium intensity. The peak amplitude was calculated as the maximum intensity divided by the initial intensity of a single cycle. The peak and decay times were defined as the time intervals during which the normalized intensity F_{norm} increases from 0.1 to 0.9⁴⁸ and decreases from 1.0 to 0.5⁴⁷, respectively. The normalized fluorescence intensity F_{norm} was calculated by the Eq. (1).

$$F_{\text{norm}}(t) = (F(t) - F_{\text{min}}) / (F_{\text{max}} - F_{\text{min}}) \quad (1)$$

where F_{max} and F_{min} represent the maximum and minimum calcium intensity in each ROI.

The electrophysiological properties of cells in the fabricated tissues were characterized by using microelectrode array (MEA) system (Tucker-Davis Technologies Inc, USA) and a computer with Synapse program. The tissues cultured for 5 days were inserted into the sterilized MEA. Recordings were conducted at 24,414 Hz with a 60 Hz notch filter, using a 0.1–300 Hz bandpass filter for local field potential and a 300–3000 Hz bandpass filter for single unit potential. The signals were obtained at the physiological environment of 37 °C and 5 % CO₂.

To evaluate the cellular response to glutamate and acetylcholine stimulation, neuromuscular tissue constructs were treated with DPBS, 300 μ M glutamate (Sigma-Aldrich), and 50 mM acetylcholine (Sigma-Aldrich). Glutamate and acetylcholine were injected after 30 seconds of treatment with DPBS and glutamate, respectively. The $[Ca^{2+}]$ transients for each ROI by glutamate and acetylcholine C_{trans} were calculated using the Eq. (2).

$$C_{\text{trans}} = \frac{\text{Average intensity for 5s after injection of glutamate or acetylcholine}}{\text{Average intensity for 5s after injection of PBS}} \quad (2)$$

To assess the effect of d-tubocurarine, 3D neuromuscular tissue constructs were treated with 1 mM d-tubocurarine (Sigma-Aldrich) for 5 min prior to glutamate and acetylcholine stimulation.

Transplantation of 3D muscle constructs into a mouse volumetric muscle loss model

All animal experiments were conducted according to protocols approved by the Institutional Animal Care and Use Committee (IACUC) of Yonsei University (permit number: IACUC-A-202201-1410-02). Mice were provided food and water ad libitum and maintained in a temperature-controlled, 12-h light/dark cycle animal care facility.

Volumetric muscle loss (VML) was induced in C67BL/6J mice (male, 7-week-old, Orientbio) as described previously⁶². After the mice were anesthetized with ketamine (100 mg/kg body weight; Yuhan, Seoul, Korea) and xylazine (10 mg/kg body weight; Bayer Korea, Ansan, Korea) by intramuscular injection, the skin of the left lower leg was incised, and the muscle was separated from the fascia. Once the

muscle was exposed, approximately 70% of the quadriceps femoris (QF) muscle was excised using a scalpel, resulting in limited endogenous regenerative ability and functional impairment^{62,113}. A 3D muscle construct with a dimension of 4 mm (x) × 8.4 mm (y) × 1.2 mm (z) was placed over the area that has been excised and fixed using a fibrin gel¹¹⁴ containing 91 mg/mL fibrinogen (Sigma-Aldrich) and 500 IU/mL thrombin (Sigma-Aldrich). After fixing the constructs, unreacted fibrin gel constituents were removed by washing with PBS. All the surgical procedures were performed in a biological safety cabinet. Mice were randomly assigned to six groups: (1) Normal (without defects); (2) iMPC+MN AB; (3) iMPC+MN R; (4) iMPC AB; (5) gel only; and (6) no treatment (NT) for histological examinations at week 1 ($n = 3$), week 6 ($n = 5$), and week 12 ($n = 5$), and functional assessments at week 4 ($n = 9-10$), week 8 ($n = 5$), and week 12 ($n = 5$).

Muscle sample collection

Tissue samples were harvested at various time points and fixed with 10% formalin solution (Sigma-Aldrich) overnight at 4 °C, followed by paraffin embedding for sectioning. The samples were sectioned in the transverse plane (thickness, 7 μm) and collected on Histobond adhesive microscope slides (Marienfeld, Lauda-Königshofen, Germany).

Histologic and immunofluorescent analyses

Hematoxylin and eosin (H&E) and Masson's trichrome (MT) staining were performed on the muscle paraffin sections to determine tissue histology using a slide scanner (VS120-S5-W, Olympus, Tokyo, Japan). The total number of nuclei centrally located in the myofibers near the defective areas was manually counted using the multipoint tool in the software Fiji¹¹⁰. The myofiber cross-sectional area (CSA) of the muscle samples was measured manually using Fiji¹¹⁰ software. Using Fiji¹¹⁰ software and MT staining images, the fibrotic area was quantified as the percentage of the area within a section that was collagen-stained.

The difference in the distribution of the CSA of myofibers of the group A versus the group B, D_{A-B} , was calculated by the Eq. (3).

$$D_{A-B} = \sqrt{\frac{(\sum_{i=1}^N (m_A^i - m_B^i)^2)}{N}} \quad (3)$$

where m_A^i and m_B^i represents the percentage value in the i th bin for groups A and B, respectively. Parameter N is the total number of bins in the histogram. The similarity of the group A versus the group B, S_{A-B} , was calculated by the Eq. (4).

$$S_{A-B} (\%) = 100 (\%) - D_{A-B} \quad (4)$$

For immunofluorescence staining, tissue sections were deparaffinized, rehydrated, and subjected to heat-induced antigen retrieval using citrate buffer (pH 6.0; Sigma-Aldrich). The samples were permeabilized using 0.25% Triton-X 100 in PBS for 20 min and then blocked with 4% BSA for 1 h. The sections were incubated overnight at 4 °C with primary antibodies (Supplementary Table 1). After incubation with antibodies, the sections were washed with PBS and incubated with fluorescently labeled secondary antibodies or Alexa Fluor 488 α-bungarotoxin for AChR. The nuclei were counterstained with 4',6-diamidino-2-phenylindole (DAPI, TCI America, Portland, OR, USA). The sections were imaged using a confocal microscope (LSM 880 and LSM 980, Carl Zeiss). The number of vessels in the defective area was measured using immunofluorescent images for CD31. AChRs and NMJs were counted using the images for which BTX-positive AChRs on the MF-positive myofibers and SV2/2H3 (synaptic vesicle 2/neurofilament)-positive neurofilaments colocalized. For all image quantification analyses, at least three random fields of view were analyzed per group using the image analysis software Fiji¹¹⁰.

Animal functional examination

To assess the skeletal muscle function of the mice, in vivo muscle electrophysiology was performed using the Whole Animal Muscle Test System (1300 A system, Aurora Scientific Inc., Aurora, ON, Canada). Mice were anesthetized with a ketamine cocktail (ketamine, xylazine, and saline mixed in a 3:2:3 volume ratio). The anesthetized mice were placed on a platform, with their left leg secured by a knee clamp, and their foot fixed onto a lever arm with a force transducer positioned at a 90° angle. Electrical stimulation was administered via two monopolar electrodes, beginning at 10 mA and gradually increasing until the maximum twitch force response was achieved. The optimal current was determined, and stimuli were then applied at frequencies of 100 Hz, 120 Hz, and 150 Hz to identify the optimal stimulation frequency. Using the determined optimal current and frequency, measurements of muscle contraction capabilities and performance were conducted. Muscle contraction was evaluated through single stimulation muscle contractions (twitch) and continuous stimuli muscle contractions (tetanus). Muscle performance was assessed by measuring the decline in performance over time through sustained continuous stimuli (fatigue), with the evaluation point set at 50% of the initial maximum contraction force. The maximum rates of contraction and relaxation were recorded throughout the procedure. Data were calculated using the Aurora 610 A: Dynamic Muscle Control Labbook (DMC v6.0, Aurora Scientific Inc.) and analyzed using Aurora 611 A and 612 A: Dynamic Muscle Analysis and High-Throughput Instruction (DMA v5.3, Aurora Scientific Inc.).

To evaluate the balanced weight bearing (WB) of the injured and uninjured hindlimbs, we conducted a WB assessment. We used a long, narrow plastic chamber (9 cm width, 71 cm length, 12.5 cm height) equipped with an electronic sensor (D Triple Co., Ltd., Gumi, Korea). Each mouse was placed in the chamber, and the WB force was measured as it passed over the electronic sensor. The WB force was recorded three times for both the injured and uninjured hindlimbs. Data collection and analysis were performed using the D-triple DWBM graph viewer (D Triple Co., Ltd., Gumi, Korea).

A grip strength meter (Bioseb, BIO-GS3, France) was used to measure the strength of the hind limb grip. Each mouse was guided towards a metal grid (100 × 80 mm, angled 20°) while being held near the base of the tail and with the scruff of the neck. After the mouse grasped the grid with its left hind paw, it was pulled down at a constant speed while maintaining the torso of the mouse parallel to the grid. The peak resistance force was captured and automatically registered in gram force by the apparatus, and the strength meter was reset to 0 g before each test and subsequent measurement. The mean force of the six trials was used for the analysis to reduce procedure-related variability.

For the open field analysis, the mice were placed in a box with the size of 30 × 30 × 30 cm. The box for the open field analysis was cleaned with 70% ethyl alcohol solution and dried in air before each trial. The motion of the mice was captured with a video camera and analyzed using the commercial software Smart Vision 2.5.21 (Panlab, Barcelona, Spain) over a period of 5 minutes.

The rotarod test was conducted to analyze the motor activity and balance of the mice using the rotarod treadmill (47600; UGO Basile, Comerio, VA, Italy). The latency duration before the mice fell from the rod, which was rotated at the rotational speed increasing from 4 to 40 rpm over 300 seconds, was measured twice for each trial.

Gait analysis was performed by visualizing the footprint of the hindfeet of the mice with non-toxic washable paint. The mice were placed at the entrance of a dark acrylic square tunnel (30 cm long × 10 cm wide × 10 cm high) over white paper. Footprints were measured one day before and 4, 8, and 12 weeks after surgery ($n = 5-10$ per group). Footprint patterns were manually measured using the Fiji¹¹⁰ software.

In situ fabrication of artificial muscle at the mouse hindlimb defect site

For in situ applications, we fabricated an acoustofluidic device and tissue mold having shape and dimensions suitable for insertion into the defect site of a VML-injured mouse hindlimb. The tissue mold and the piezoelectric device were coupled with the 100 μm -thick rubber film to prevent the detachment of the mold during the in situ fabrication.

Cells stained with fluorescent membrane dye (CellMask; Invitrogen) were mixed with a fibrinogen solution. The pre-gel solution with cells was then mixed with thrombin solution and transferred into the tissue mold placed at the defect site, followed by the application of acoustofluidic cues for 2 min. After additional gelation for 6 min, the acoustofluidic device was removed from the injured region. The final fibrinogen and thrombin concentrations were 4 mg/mL and 8 U/mL, respectively. The density of the cells in the mixed solution was 1×10^7 cells/mL.

Fluorescent images of cells in the fabricated tissue at the VML site were obtained using an upright epifluorescence microscope (Ni-U, Nikon) and a complementary metal-oxide-semiconductor (CMOS) camera (DS-Qi2, Nikon).

Human iPSCs

The use of human iPSCs was approved by the Institutional Review Board (IRB) of Yonsei University (Permit Number: 7001988-202304-BR-1866-01E). The human KYOU-DXR0109B (ACS-1023, American Type Culture Collection, Manassas, VA, USA) was used for hiPSC-NPCs (neural progenitor cells) and hiPSC-SKMs (skeletal muscle cells) differentiation. hiPSCs were cultured in Matrigel-coated dishes (Corning) with mTeSR-Plus (STEMCELL Technologies) and passaged using ReLeSR (STEMCELL Technologies). The cells were regularly checked for mycoplasma contamination using the MycoAlert PLUS Mycoplasma Detection Kit (Lonza) and the infection was prevented using the Myco-Guard™ Mycoplasma Elimination Reagent (Biomax).

Differentiation of hiPSC-NPCs, hiPSC-Motor Neurons, and hiPSC-SKMs

The differentiation of hiPSCs into NPCs was conducted as previously reported¹¹⁵ with minor modifications. The 70–80% confluent hiPSCs were dissociated into single cells using TryPLE Express Enzyme (Thermo Fisher Scientific) and transferred to an ultra-low attachment 6-well plate (Corning) in mTeSR-Plus medium supplemented with 3 μM CHIR99021 (LC Laboratories), 10 μM SB-431542 (Tocris), 2.5 μM dorsomorphin (Sigma-Aldrich), 500 nM purmorphamine (STEMCELL Technologies), and 10 μM ROCK inhibitor Y-27632 (BioGems). After two days, the medium was replaced by a medium comprising DMEM/F12 (Thermo Fisher Scientific) and Neurobasal (Thermo Fisher Scientific) in a 1:1 ratio, supplemented with 1:200 (v/v) N2 supplement (Thermo Fisher Scientific), 1:100 (v/v) B27 supplement without retinoic acid (Thermo Fisher Scientific), 3 μM CHIR99021 (LC Laboratories), 10 μM SB-431542 (Tocris), 2.5 μM dorsomorphin (Sigma-Aldrich), and 500 nM purmorphamine (STEMCELL Technologies). After another two days, the medium was switched to NPC maintenance medium comprising DMEM/F12 (Thermo Fisher Scientific) and Neurobasal (Thermo Fisher Scientific) in a 1:1 ratio, supplemented with 1:200 (v/v) N2 supplement (Thermo Fisher Scientific), 1:100 (v/v) B27 supplement without retinoic acid (Thermo Fisher Scientific), 3 μM CHIR99021 (LC Laboratories), 500 nM purmorphamine (STEMCELL Technologies), and ascorbic acid (Sigma-Aldrich). After a week, the cells were split into single cells and cultured in NPC medium, which was replaced every other day. When confluence reached 80%, NPCs were split at ratios ranging from 1:5 to 1:10.

The iPSC-motor neurons (hiPSC-MNs) were differentiated into motor neurons according to a previously reported protocol¹⁷⁵ with minor modifications. The 70–80% confluent hiPSC-NPCs were

dissociated into single cells using TryPLE Express Enzyme and transferred to Matrigel-coated culture dishes with NPC medium. When confluency reached 70%, 0.1 μM retinoic acid (Sigma) was added to the NPC medium, which was replaced every 2–3 days. After 7 days, 1 μM purmorphamine was additionally supplemented to the NPC medium, which was replaced every 2–3 days for another 7 days.

The skeletal muscle cells were differentiated from hiPSCs according to a previously published protocol⁷⁴ with slight modifications. The 70–80% confluent iPSCs were dissociated into single cells using TryPLE Express Enzyme and transferred to Matrigel-coated culture dishes at a density of 1.4×10^5 cells/mL with mTeSR-Plus medium containing 10 μM Y-27632 for one day. When confluency reached to 15–20%, the medium was switched to a differentiation medium comprising DMEM/F12 supplemented with 1:100 (v/v) Insulin-Transferrin-Selenium (ITS, Thermo Fisher Scientific), 1:100 (v/v) non-essential amino acids (NEAA, Thermo Fisher Scientific), 1:100 (v/v) penicillin-streptomycin (P/S, Thermo Fisher Scientific), 3 μM CHIR99021 (LC Laboratories), and 0.5 μM LDN-193189 (Sigma), which was replaced daily for 3 days. On day 3 of differentiation, 20 ng/mL basic fibroblast growth factor (bFGF, Peprotech) was added for additional 3 days. After 6 days, the medium was changed to a DMEM/F12-based medium supplemented with 15% (v/v) Knock-Out Serum Replacement (KSR, Thermo Fisher Scientific), 1:100 (v/v) non-essential amino acids (NEAA, Thermo Fisher Scientific), 1:100 (v/v) penicillin-streptomycin (P/S, Thermo Fisher Scientific), 0.1 mM β -mercaptoethanol (Sigma), 10 ng/mL hepatocyte growth factor, (HGF, Peprotech), 2 ng/mL IGF-1 (Peprotech), 20 ng/mL bFGF (Peprotech), and 0.5 μM LDN-193189 (Sigma) for 3 days. After day 9 of differentiation, cells were cultured in a medium consisting of DMEM/F12 containing 15% (v/v) Knock-Out Serum Replacement (KSR, Thermo Fisher Scientific), 1:100 (v/v) non-essential amino acids (NEAA, Thermo Fisher Scientific), 1:100 (v/v) penicillin-streptomycin (P/S, Thermo Fisher Scientific), 0.1 mM β -mercaptoethanol (Sigma), 10 ng/mL HGF (Peprotech), and 2 ng/mL IGF-1 (Peprotech). The medium was replaced every day until day 12, and then every other day for another 2 weeks. The differentiated myogenic cells were passaged and cryopreserved for subsequent use.

Isolation of the spinal cord from an adult mouse

The spinal cord was isolated from C67BL/6J mice (male, 7-week-old, Orientbio) as described previously¹¹⁶. The mice were anesthetized with ketamine (100 mg/kg body weight) and xylazine (10 mg/kg body weight) via intramuscular injection. The spinal column was separated by opening the fur along the spinal column distally and cutting both sides along the spinal column past the pelvic bone. The spinal column was cut distally to the pelvic bone and trimmed until the spinal cord was visible. A pipette tip with a 10 mL syringe filled with ice-cold PBS was inserted into the most distal end of the spine, and the spinal cord was extruded by applying constant pressure. The isolated spinal cords were stored in ice-cold PBS until further experiments were performed.

In situ fabrication of neural tissue constructs at the spinal cord defect site

hiPSC-NPCs were suspended in fibrinogen solution. The cell-laden gel solution was mixed with thrombin solution and transferred into the tissue mold. The concentrations of fibrinogen and thrombin in the mixed solution were 4 mg/mL and 8 U/mL, respectively. The density of the hiPSC-NPCs in the solution was 1×10^7 cells/mL. The acoustofluidic cues were applied for 2 min. After an additional incubation for 10 min at 37°C, the tissue constructs were incubated in NPC maintenance medium for five days.

Fabrication of vascular tissues

Human umbilical vein endothelial cells (HUVECs; Lonza, Basel, Switzerland) were mixed with fibrinogen solution at a density of 1×10^7 cells/mL. The cell-laden mixture solution was transferred into the tissue mold

after adding the thrombin solution. The acoustofluidic cues were applied for 2.5 min. The concentrations of fibrinogen and thrombin in the mixed solution were 2.5 mg/mL and 0.8 U/mL, respectively. Tissues with arranged HUVECs were cultivated in the endothelial cell growth medium-2 (EGM-2; Lonza) culture medium.

Fabrication of tissues with isotropic and anisotropic ECM collagen arrangement

Cells stained with the fluorescent membrane dye (Invitrogen) were suspended in a mixture of high-concentration collagen solution (Corning), 10X PBS, and DI water. A 1N sodium hydroxide (Duksan Chemical, Korea) solution was added to the collagen-cell mixture to initiate the gelation process at a constant pH of 7.4. The final concentration of collagen was 4 mg/mL, and the cell density was 1×10^7 cells/mL.

The pre-gel solution was then transferred into the tissue mold, and an acoustofluidic cue was applied for 15 min. Fibers and thick bundles of collagen were formed by polymerizing collagen at 37°C and 22°C, respectively¹¹⁷. Confocal reflectance microscopy was used to visualize collagen¹¹⁸.

Cardiac organoid with aligned vasculature

To generate chemically induced cardiac organoids, pMEFs were seeded in an ultra-low-attachment 96-well plate (Corning) at 8000 cells/well. The following day, the medium was replaced every day with cardiac reprogramming medium containing DMEM/F12 (Thermo Fisher Scientific) supplemented with 15% FBS (Thermo Fisher Scientific), 5% knockout serum replacement (Thermo Fisher Scientific), 1% (v/v) NEAA (Thermo Fisher Scientific), 1% (v/v) penicillin-streptomycin (Thermo Fisher Scientific), 0.1% β -mercaptoethanol (Thermo Fisher Scientific), 10 μ M CHIR99021 (LC Laboratory, Woburn, MA, USA), 2 μ M A83-01 (Tocris Bioscience, Bristol, UK), 15 μ M Forskolin (LC Laboratory), and 1 μ M SC-1 (Cayman Chemical, Ann Arbor, MI, USA) for 5 days.

Cardiac organoids, HUVECs, and fibrinogen solution were mixed. After injecting thrombin solution, the cell-laden hydrogel solution was transferred into the mold. The density of HUVECs in the solution was 1×10^7 cells/mL. The number of cardiac organoids was 2–3 for each tissue construct having a size of $4 \times 8 \times 0.8$ mm. The final concentrations of the fibrinogen and thrombin were 2.5 mg/mL and 0.8 U/mL, respectively. The acoustofluidic cues were applied for 5 min. The fabricated tissues were cultured for 3 days in a culture media composed of a 3:1 mixture of EGM2 and cardiac reprogramming medium.

Statistics and reproducibility

Statistical significance was determined using unpaired Student's t-tests and one-way or two-way analysis of variance (ANOVA) using GraphPad Prism software (GraphPad Software, San Diego, CA, USA). All data are presented as mean \pm standard deviation. Exact *p* values are presented in Source Data. The experiments to obtain microscopic images were independently replicated four times, exhibiting similar results.

Reporting summary

Further information on research design is available in the Nature Portfolio Reporting Summary linked to this article.

Data availability

The data generated in this study are provided in the Supplementary Information and Source Data file. Source data are provided with this paper.

References

- Ingber, D. E. Human organs-on-chips for disease modelling, drug development and personalized medicine. *Nat. Rev. Genet.* **23**, 467–491 (2022).
- Monteiro, M. V., Zhang, Y. S., Gaspar, V. M. & Mano, J. F. 3D-bioprinted cancer-on-a-chip: level-up organotypic in vitro models. *Trends Biotechnol.* **40**, 432–447 (2022).
- Fatehullah, A., Tan, S. H. & Barker, N. Organoids as an in vitro model of human development and disease. *Nat. Cell Biol.* **18**, 246–254 (2016).
- Mota, C., Camarero-Espinosa, S., Baker, M. B., Wieringa, P. & Moroni, L. Bioprinting: from tissue and organ development to in vitro models. *Chem. Rev.* **120**, 10547–10607 (2020).
- Gupta, A., Lutolf, M. P., Hughes, A. J. & Sonnen, K. F. Bioengineering in vitro models of embryonic development. *Stem Cell Rep.* **16**, 1104–1116 (2021).
- Walma, D. A. C. & Yamada, K. M. The extracellular matrix in development. *Development* **147**, dev175596 (2020).
- Gros, J., Scaal, M. & Marcelle, C. A two-step mechanism for myotome formation in chick. *Developmental Cell* **6**, 875–882 (2004).
- Goody, M. F., Sher, R. B. & Henry, C. A. Hanging on for the ride: Adhesion to the extracellular matrix mediates cellular responses in skeletal muscle morphogenesis and disease. *Developmental Biol.* **401**, 75–91 (2015).
- Ruiz-Gómez, M., Coutts, N., Price, A., Taylor, M. V. & Bate, M. *Drosophila* dumbfounded: A myoblast attractant essential for fusion. *Cell* **102**, 189–198 (2000).
- Abmayr, S. M. & Pavlath, G. K. Myoblast fusion: lessons from flies and mice. *Development* **139**, 641–656 (2012).
- Sieiro-Mosti, D., De La Celle, M., Pelé, M. & Marcelle, C. A dynamic analysis of muscle fusion in the chick embryo. *Development* **141**, 3605–3611 (2014).
- Krauss, R. S., Joseph, G. A. & Goel, A. J. Keep your friends close: Cell–cell contact and skeletal myogenesis. *Cold Spring Harb. Perspect. Biol.* **9**, 029298 (2017).
- Barbeau, S., Tahraoui-Bories, J., Legay, C. & Martinat, C. Building neuromuscular junctions in vitro. *Development* **147**, dev193920 (2020).
- Guarino, S. R., Canciani, A. & Forneris, F. Dissecting the extracellular complexity of neuromuscular junction organizers. *Front. Mol. Biosci.* **6**, 00156 (2020).
- Li, L., Xiong, W.-C. & Mei, L. Neuromuscular junction formation, aging, and disorders. *Annu. Rev. Physiol.* **80**, 159–188 (2018).
- Osaki, T., Uzel, S. G. M. & Kamm, R. D. Microphysiological 3D model of amyotrophic lateral sclerosis (ALS) from human iPS-derived muscle cells and optogenetic motor neurons. *Sci. Adv.* **4**, eaat5847 (2018).
- Dejana, E. Endothelial cell–cell junctions: happy together. *Nat. Rev. Mol. Cell Biol.* **5**, 261–270 (2004).
- Heinke, J., Patterson, C. & Moser, M. Life is a pattern: vascular assembly within the embryo. *FBE* **4**, 2269–2288 (2012).
- Buchsbaum, I. Y. & Cappello, S. Neuronal migration in the CNS during development and disease: insights from in vivo and in vitro models. *Development* **146**, dev163766 (2019).
- Rahimi-Balaei, M., Bergen, H., Kong, J. & Marzban, H. Neuronal migration during development of the cerebellum. *Front. Cell. Neurosci.* **12**, 00484 (2018).
- Cho, S., Discher, D. E., Leong, K. W., Vunjak-Novakovic, G. & Wu, J. C. Challenges and opportunities for the next generation of cardiovascular tissue engineering. *Nat. Methods* **19**, 1064–1071 (2022).
- Park, S. E. et al. Geometric engineering of organoid culture for enhanced organogenesis in a dish. *Nat. Methods* **19**, 1449–1460 (2022).
- Bliley, J. M., Shiwardski, D. J. & Feinberg, A. W. 3D-bioprinted human tissue and the path toward clinical translation. *Sci. Transl. Med.* **14**, eabo7047 (2022).

24. Choi, S. et al. Fibre-infused gel scaffolds guide cardiomyocyte alignment in 3D-printed ventricles. *Nat. Mater.* **22**, 1039–1046 (2023).
25. Bernal, P. N. et al. Volumetric bioprinting of complex living-tissue constructs within seconds. *Adv. Mater.* **31**, 1904209 (2019).
26. Zhang, T. et al. Bioink design for extrusion-based bioprinting. *Appl. Mater. Today* **25**, 101227 (2021).
27. Lee, M., Rizzo, R., Surman, F. & Zenobi-Wong, M. Guiding lights: tissue bioprinting using photoactivated materials. *Chem. Rev.* **120**, 10950–11027 (2020).
28. Gillispie, G. et al. Assessment methodologies for extrusion-based bioink printability. *Biofabrication* **12**, 022003 (2020).
29. Rufo, J., Cai, F., Friend, J., Wiklund, M. & Huang, T. J. Acoustofluidics for biomedical applications. *Nat. Rev. Methods Prim.* **2**, 30 (2022).
30. Bruus, H. Acoustofluidics 7: The acoustic radiation force on small particles. *Lab a Chip* **12**, 1014–1021 (2012).
31. Kang, B. et al. High-resolution acoustophoretic 3D cell patterning to construct functional collateral cylindroids for ischemia therapy. *Nat. Commun.* **9**, 5402 (2018).
32. Poisson, J. et al. Liver sinusoidal endothelial cells: physiology and role in liver diseases. *J. Hepatol.* **66**, 212–227 (2017).
33. Pazzaglia, U. E., Congiu, T., Marchese, M., Spagnuolo, F. & Quacci, D. Morphometry and patterns of lamellar bone in human haversian systems. *Anat. Rec.* **295**, 1421–1429 (2012).
34. Shin, J. et al. Three-dimensional electroconductive hyaluronic acid hydrogels incorporated with carbon nanotubes and polypyrrole by catechol-mediated dispersion enhance neurogenesis of human neural stem cells. *Biomacromolecules* **18**, 3060–3072 (2017).
35. Zhen, S. & Li, X. Liposomal delivery of CRISPR/Cas9. *Cancer Gene Ther.* **27**, 515–527 (2020).
36. Wohlgemuth, R. P., Brashear, S. E. & Smith, L. R. Alignment, cross linking, and beyond: a collagen architect's guide to the skeletal muscle extracellular matrix. *Am. J. Physiol.-Cell Physiol.* **325**, C1017–C1030 (2023).
37. Garofalo, F., Laurell, T. & Bruus, H. Performance study of acoustophoretic microfluidic silicon-glass devices by characterization of material- and geometry-dependent frequency spectra. *Phys. Rev. Appl.* **7**, 054026 (2017).
38. Kim, M., Barnkob, R. & Meacham, J. M. Rapid measurement of the local pressure amplitude in microchannel acoustophoresis using motile cells. *J. Acoustical Soc. Am.* **150**, 1565–1576 (2021).
39. Wang, H., Yang, Y., Liu, J. & Qian, L. Direct cell reprogramming: approaches, mechanisms and progress. *Nat. Rev. Mol. Cell Biol.* **22**, 410–424 (2021).
40. Jin, Y. & Cho, S.-W. Bioengineering platforms for cell therapeutics derived from pluripotent and direct reprogramming. *APL Bioeng.* **5**, 031501 (2021).
41. Rao, L., Qian, Y., Khodabukus, A., Ribar, T. & Bursac, N. Engineering human pluripotent stem cells into a functional skeletal muscle tissue. *Nat. Commun.* **9**, 126 (2018).
42. Iberite, F., Gruppioni, E. & Ricotti, L. Skeletal muscle differentiation of human iPSCs meets bioengineering strategies: perspectives and challenges. *npj Regenerative Med.* **7**, 23 (2022).
43. Raman, R. et al. Optogenetic skeletal muscle-powered adaptive biological machines. *Proc. Natl Acad. Sci. USA* **113**, 3497–3502 (2016).
44. Kuo, I. Y. & Ehrlich, B. E. Signaling in Muscle Contraction. *Cold Spring Harb. Perspect. Biol.* **7**, 006023 (2015).
45. Silva, A. C. et al. Co-emergence of cardiac and gut tissues promotes cardiomyocyte maturation within human iPSC-derived organoids. *Cell Stem Cell* **28**, 2137–2152.e2136 (2021).
46. Han, J., Wu, Q., Xia, Y., Wagner, M. B. & Xu, C. Cell alignment induced by anisotropic electrospun fibrous scaffolds alone has limited effect on cardiomyocyte maturation. *Stem Cell Res.* **16**, 740–750 (2016).
47. Kuo, P.-L. et al. Myocyte shape regulates lateral registry of sarcomeres and contractility. *Am. J. Pathol.* **181**, 2030–2037 (2012).
48. Capote, J., Bolaños, P., Schuhmeier, R. P., Melzer, W. & Caputo, C. Calcium transients in developing mouse skeletal muscle fibres. *J. Physiol.* **564**, 451–464 (2005).
49. Lo, H. P. et al. Cavin4 interacts with Bin1 to promote T-tubule formation and stability in developing skeletal muscle. *J. Cell Biol.* **220**, e201905065 (2021).
50. Kim, M. et al. Multimodal characterization of cardiac organoids using integrations of pressure-sensitive transistor arrays with three-dimensional liquid metal electrodes. *Nano Lett.* **22**, 7892–7901 (2022).
51. Zhu, M. et al. Flexible electrodes for in vivo and in vitro electrophysiological signal recording. *Adv. Healthc. Mater.* **10**, 2100646 (2021).
52. Chung, W. G. et al. Recent advances in electrophysiological recording platforms for brain and heart organoids. *Adv. Nano-Biomed Res.* **2**, 2200081 (2022).
53. Vila, O. F., Qu, Y. & Vunjak-Novakovic, G. In vitro models of neuromuscular junctions and their potential for novel drug discovery and development. *Expert Opin. Drug Discov.* **15**, 307–317 (2020).
54. Schmidt, M., Schüller, S. C., Hüttner, S. S., von Eyss, B. & von Maltzahn, J. Adult stem cells at work: regenerating skeletal muscle. *Cell. Mol. Life Sci.* **76**, 2559–2570 (2019).
55. Folker, E. & Baylies, M. Nuclear positioning in muscle development and disease. *Front. Physiol.* **4**, 00363 (2013).
56. Forcina, L., Cosentino, M. & Musarò, A. Mechanisms regulating muscle regeneration: insights into the interrelated and time-dependent phases of tissue healing. *Cells* **9**, 1297 (2020).
57. Maffioletti, S. M., Novello, M., English, K. & Tedesco, F. S. Stem cell transplantation for muscular dystrophy: The challenge of immune response. *BioMed. Res. Int.* **2014**, 964010 (2014).
58. Desgeorges, T. et al. Open-CSAM, a new tool for semi-automated analysis of myofiber cross-sectional area in regenerating adult skeletal muscle. *Skelet. Muscle* **9**, 2 (2019).
59. Gilbert-Honick, J. & Grayson, W. Vascularized and innervated skeletal muscle tissue engineering. *Adv. Healthc. Mater.* **9**, 1900626 (2020).
60. Giudice, J. & Taylor, J. M. Muscle as a paracrine and endocrine organ. *Curr. Opin. Pharmacol.* **34**, 49–55 (2017).
61. Quarta, M. et al. Bioengineered constructs combined with exercise enhance stem cell-mediated treatment of volumetric muscle loss. *Nat. Commun.* **8**, 15613 (2017).
62. Jin, Y. et al. Functional skeletal muscle regeneration with thermally drawn porous fibers and reprogrammed muscle progenitors for volumetric muscle injury. *Adv. Mater.* **33**, 2007946 (2021).
63. Kim, H. Y., Wang, J., Chung, K. & Chung, J. M. A surgical ankle sprain pain model in the rat: Effects of morphine and indomethacin. *Neurosci. Lett.* **442**, 161–164 (2008).
64. Seo, J. H. et al. DNA double-strand break-free CRISPR interference delays huntington's disease progression in mice. *Commun. Biol.* **6**, 466 (2023).
65. Samandari, M., Mostafavi, A., Quint, J., Memić, A. & Tamayol, A. In situ bioprinting: intraoperative implementation of regenerative medicine. *Trends Biotechnol.* **40**, 1229–1247 (2022).
66. Iordachescu, A., Eisenstein, N. & Appleby-Thomas, G. Space habitats for bioengineering and surgical repair: addressing the requirement for reconstructive and research tissues during deep-space missions. *npj Microgravity* **9**, 23 (2023).
67. Inoue, M. et al. Current status and prospects of regenerative medicine for spinal cord injury using human induced pluripotent stem cells: a review. *Stem Cell Investig.* **10**, 6 (2023).

68. Wu, Y., Ravnic, D. J. & Ozbolat, I. T. Intraoperative bioprinting: Repairing tissues and organs in a surgical setting. *Trends Biotechnol.* **38**, 594–605 (2020).
69. Erharter, A., Rizzi, S., Mertens, J. & Edenhofer, F. Take the shortcut – direct conversion of somatic cells into induced neural stem cells and their biomedical applications. *FEBS Lett.* **593**, 3353–3369 (2019).
70. Zhang, Y. X., Chen, S. L., Li, Y. M. & Zheng, Y. W. Limitations and challenges of direct cell reprogramming in vitro and in vivo. *Histol. Histopathol.* **37**, 723–737 (2022).
71. Cantor, E. L. et al. Passage number affects differentiation of sensory neurons from human induced pluripotent stem cells. *Sci. Rep.* **12**, 15869 (2022).
72. Kimbrel, E. A. & Lanza, R. Current status of pluripotent stem cells: moving the first therapies to the clinic. *Nat. Rev. Drug Discov.* **14**, 681–692 (2015).
73. Chal, J. et al. Differentiation of pluripotent stem cells to muscle fiber to model duchenne muscular dystrophy. *Nat. Biotechnol.* **33**, 962–969 (2015).
74. Chal, J. et al. Generation of human muscle fibers and satellite-like cells from human pluripotent stem cells in vitro. *Nat. Protoc.* **11**, 1833–1850 (2016).
75. Stacpoole, S. R. L. et al. Efficient derivation of NPCs, spinal motor neurons and midbrain dopaminergic neurons from hESCs at 3% oxygen. *Nat. Protoc.* **6**, 1229–1240 (2011).
76. Guo, X., Badu-Mensah, A., Thomas, M. C., McAleer, C. W. & Hickman, J. J. Characterization of functional human skeletal myotubes and neuromuscular junction derived—from the same induced pluripotent stem cell source. *Bioengineering* **7**, 133 (2020).
77. Yang, S. et al. Harmonic acoustics for dynamic and selective particle manipulation. *Nat. Mater.* **21**, 540–546 (2022).
78. Armingol, E., Officer, A., Harismendy, O. & Lewis, N. E. Deciphering cell–cell interactions and communication from gene expression. *Nat. Rev. Genet.* **22**, 71–88 (2021).
79. Collins, D. J. et al. Two-dimensional single-cell patterning with one cell per well driven by surface acoustic waves. *Nat. Commun.* **6**, 8686 (2015).
80. Gu, L. et al. Size- and density-dependent acoustic differential bioassembly of spatially-defined heterocellular architecture. *Biofabrication* **15**, 015019 (2023).
81. Melde, K., Mark, A. G., Qiu, T. & Fischer, P. Holograms for acoustics. *Nature* **537**, 518–522 (2016).
82. Lee, J., Rhyou, C., Kang, B. & Lee, H. Continuously phase-modulated standing surface acoustic waves for separation of particles and cells in microfluidic channels containing multiple pressure nodes. *J. Phys. D: Appl. Phys.* **50**, 165401 (2017).
83. Li, P. et al. Acoustic separation of circulating tumor cells. *Proc. Natl Acad. Sci. USA* **112**, 4970–4975 (2015).
84. Xu, F. et al. The assembly of cell-encapsulating microscale hydrogels using acoustic waves. *Biomaterials* **32**, 7847–7855 (2011).
85. Pavlic, A., Nagpure, P., Ermanni, L. & Dual, J. Influence of particle shape and material on the acoustic radiation force and microstreaming in a standing wave. *Phys. Rev. E* **106**, 015105 (2022).
86. Chansoria, P., Narayanan, L. K., Schuchard, K. & Shirwaiker, R. Ultrasound-assisted biofabrication and bioprinting of preferentially aligned three-dimensional cellular constructs. *Biofabrication* **11**, 035015 (2019).
87. Asif, S., Chansoria, P. & Shirwaiker, R. Ultrasound-assisted vat photopolymerization 3D printing of preferentially organized carbon fiber reinforced polymer composites. *J. Manuf. Process.* **56**, 1340–1343 (2020).
88. Agrawal, P., Zhuang, S., Dreher, S., Mitter, S. & Ahmed, D. SonoPrint: Acoustically Assisted Volumetric 3D Printing for Composites. *bioRxiv*, 2023.2008.2007.552292 (2023).
89. Chansoria, P., Asif, S., Gupta, N., Piedrahita, J. & Shirwaiker, R. A. Multiscale Anisotropic Tissue Biofabrication via Bulk Acoustic Patterning of Cells and Functional Additives in Hybrid Bioinks. *Adv. Healthc. Mater.* **11**, 2102351 (2022).
90. Hu, X. et al. Smart acoustic 3D cell construct assembly with high-resolution. *Biofabrication* **14**, 045003 (2022).
91. Deshmukh, D. V. et al. Continuous production of acoustically patterned cells within hydrogel fibers for musculoskeletal tissue engineering. *Adv. Funct. Mater.* **32**, 2113038 (2022).
92. Davoodi, E. et al. Extrusion and microfluidic-based bioprinting to fabricate biomimetic tissues and organs. *Adv. Mater. Technol.* **5**, 1901044 (2020).
93. Wu, D. et al. Biomolecular actuators for genetically selective acoustic manipulation of cells. *Sci. Adv.* **9**, eadd9186 (2023).
94. Ren, T., Chen, P., Gu, L., Ogut, M. G. & Demirci, U. Soft ring-shaped cellu-robots with simultaneous locomotion in batches. *Adv. Mater.* **32**, 1905713 (2020).
95. Wang, J. et al. Rational design and acoustic assembly of human cerebral cortex-like microtissues from hiPSC-derived neural progenitors and neurons. *Adv. Mater.* **35**, 2210631 (2023).
96. Kang, B. et al. Role of mechanical flow for actin network organization. *Acta Biomaterialia* **90**, 217–224 (2019).
97. Kang, B. et al. Spatial regulation of hydrogel polymerization reaction using ultrasound-driven streaming vortex. *Ultrason. Sonochem.* **110**, 107053 (2024).
98. Tan, J. et al. Hydrogel protection strategy to stabilize water-splitting photoelectrodes. *Nat. Energy* **7**, 537–547 (2022).
99. Kang, B. et al. Stable water splitting using photoelectrodes with a cryogelated overlayer. *Nat. Commun.* **15**, 1495 (2024).
100. Walsh, D. I. III, Kong, D. S., Murthy, S. K. & Carr, P. A. Enabling microfluidics: From clean rooms to makerspaces. *Trends Biotechnol.* **35**, 383–392 (2017).
101. Baek, J., Kang, B., Rhyou, C. & Lee, H. Effect of the sound speed mismatch between fluid and channel on the particle alignment in a standing surface acoustic wave device. *Sens. Actuators B: Chem.* **346**, 130442 (2021).
102. Jin, Y. et al. Reconstruction of muscle fascicle-like tissues by anisotropic 3D patterning. *Adv. Funct. Mater.* **31**, 2006227 (2021).
103. Wiese, S. et al. Isolation and enrichment of embryonic mouse motoneurons from the lumbar spinal cord of individual mouse embryos. *Nat. Protoc.* **5**, 31–38 (2010).
104. Conrad, R. et al. Lectin-based isolation and culture of mouse embryonic motoneurons. *J. Vis. Exp.* **55**, e3200 (2011).
105. Bar-Nur, O. et al. Direct reprogramming of mouse fibroblasts into functional skeletal muscle progenitors. *Stem Cell Rep.* **10**, 1505–1521 (2018).
106. Huang, Y.-C., Dennis, R. G., Larkin, L. & Baar, K. Rapid formation of functional muscle in vitro using fibrin gels. *J. Appl. Physiol.* **98**, 706–713 (2005).
107. de Melo, B. A. G. et al. Strategies to use fibrinogen as bioink for 3D bioprinting fibrin-based soft and hard tissues. *Acta Biomaterialia* **117**, 60–76 (2020).
108. Baudoin, M. et al. Spatially selective manipulation of cells with single-beam acoustical tweezers. *Nat. Commun.* **11**, 4244 (2020).
109. Baudoin, M. et al. Folding a focalized acoustical vortex on a flat holographic transducer: Miniaturized selective acoustical tweezers. *Sci. Adv.* **5**, eaav1967 (2019).
110. Schindelin, J. et al. Fiji: an open-source platform for biological-image analysis. *Nat. Methods* **9**, 676–682 (2012).
111. Imashiro, C. et al. Propagating acoustic waves on a culture substrate regulate the directional collective cell migration. *Microsyst. Nanoengineering* **7**, 90 (2021).
112. Thielicke, W. & Stamhuis, E. PIVlab—towards user-friendly, affordable and accurate digital particle image velocimetry in MATLAB. *J. Open Res. Softw.* **2**, e30 (2014).

113. Shi, Y. et al. Self-curling 3D oriented scaffolds from fish scales for skeletal muscle regeneration. *Biomater. Res.* **26**, 87 (2022).
114. He, C. et al. Fabricating tissues in situ with the controlled cellular alignments. *Adv. Healthc. Mater.* **11**, 2100934 (2022).
115. Lorenz, C. et al. Human iPSC-derived neural progenitors are an effective drug discovery model for neurological mtDNA disorders. *Cell Stem Cell* **20**, 659–674.e659 (2017).
116. Au Richner, M., Au Jager, S. B., Au Siupka, P. & Au Vaegter, C. B. Hydraulic Extrusion of the Spinal Cord and Isolation of Dorsal Root Ganglia in Rodents. *J. Vis. Exp.* **119**, e55226 (2017).
117. Jansen, K. A. et al. The role of network architecture in collagen mechanics. *Biophysical J.* **114**, 2665–2678 (2018).
118. Yang, Y.-I. & Kaufman, L. J. Rheology and confocal reflectance microscopy as probes of mechanical properties and structure during collagen and collagen/hyaluronan self-assembly. *Biophysical J.* **96**, 1566–1585 (2009).

Acknowledgements

This work was supported by the National Research Foundation (NRF) of Korea grant (Nos. RS-2021-NR059302 and RS-2021-NR059722) funded by the Ministry of Science and ICT. This work was also supported by the Alchemist Project 2410005238 (20012378) funded by the Ministry of Trade, Industry & Energy (MOTIE, Korea), and the Institute for Basic Science (IBS-R026-D1). This work was also supported by the Yonsei Signature Research Cluster Program of 2024-22-0165, the Yonsei Fellow Program funded by Lee Youn Jae, and the Institute of Convergence Science (ICONS) at Yonsei University.

Author contributions

B.K., E.J., S.-W.C., and H.L. designed the research project. B.K. and E.J. conducted in vitro experiments, analyzed the data, and drafted the manuscript. E.J., S.Y.H., J.H.H., J.H.S., J.K., Y.J., and S.-R.C. performed the animal tests. D.K. conducted a simulation-based analysis. S.Y.H., Y.L., S.C., Y.C., Ji. Lee, and Ju. Lee supported the experiments and analysis. Y.-H.H. and D.-E.K. characterized the system. I.J., E.K., J.H.H. J.-U.P., and Y.J. conducted in vitro and in vivo electrophysiology analysis. S.-W.C. and H.L. supervised the project. B.K., E.J., S.-W.C., and H.L. wrote the manuscript.

Competing interests

S.-W.C. is a chief technology officer (CTO) of Cellartgen, Inc., Republic of Korea. The remaining authors declare no competing interests.

Additional information

Supplementary information The online version contains supplementary material available at <https://doi.org/10.1038/s41467-025-59026-4>.

Correspondence and requests for materials should be addressed to Seung-Woo Cho or Hyungsuk Lee.

Peer review information *Nature Communications* thanks Pu Chen, and the other, anonymous, reviewer(s) for their contribution to the peer review of this work. A peer review file is available.

Reprints and permissions information is available at <http://www.nature.com/reprints>

Publisher's note Springer Nature remains neutral with regard to jurisdictional claims in published maps and institutional affiliations.

Open Access This article is licensed under a Creative Commons Attribution-NonCommercial-NoDerivatives 4.0 International License, which permits any non-commercial use, sharing, distribution and reproduction in any medium or format, as long as you give appropriate credit to the original author(s) and the source, provide a link to the Creative Commons licence, and indicate if you modified the licensed material. You do not have permission under this licence to share adapted material derived from this article or parts of it. The images or other third party material in this article are included in the article's Creative Commons licence, unless indicated otherwise in a credit line to the material. If material is not included in the article's Creative Commons licence and your intended use is not permitted by statutory regulation or exceeds the permitted use, you will need to obtain permission directly from the copyright holder. To view a copy of this licence, visit <http://creativecommons.org/licenses/by-nc-nd/4.0/>.

© The Author(s) 2025

¹School of Mechanical Engineering, Yonsei University, Seoul 03722, Republic of Korea. ²Department of Biotechnology, Yonsei University, Seoul 03722, Republic of Korea. ³Department of Biomaterials Science and Engineering, Yonsei University, Seoul 03722, Republic of Korea. ⁴Department of Physiology, Yonsei University College of Medicine, Seoul 03722, Republic of Korea. ⁵Department and Research Institute of Rehabilitation Medicine, Yonsei University College of Medicine, Seoul 03722, Republic of Korea. ⁶Graduate Program of Biomedical Engineering, Yonsei University College of Medicine, Seoul 03722, Republic of Korea. ⁷Department of Materials Science and Engineering, Yonsei University, Seoul 03722, Republic of Korea. ⁸Center for Nanomedicine, Institute for Basic Science (IBS), Seoul 03722, Republic of Korea. ⁹Department of Neurosurgery, Yonsei University College of Medicine, Seoul 03722, Republic of Korea. ¹⁰Graduate Program of Nano Biomedical Engineering (NanoBME), Advanced Science Institute, Yonsei University, Seoul 03722, Republic of Korea. ¹¹Rehabilitation Institute of Neuromuscular Disease, Yonsei University College of Medicine, Seoul 03722, Republic of Korea. ¹²Department of Rehabilitation Medicine, Graduate School of Medical Science, Brain Korea 21 Project, Yonsei University College of Medicine, Seoul 03722, Republic of Korea. ¹³Brain research institute, Yonsei University College of Medicine, Seoul 03722, Republic of Korea. ¹⁴These authors contributed equally: Byungjun Kang, Eunseon Jeong.

✉ e-mail: seungwoocho@yonsei.ac.kr; hyungsuk@yonsei.ac.kr